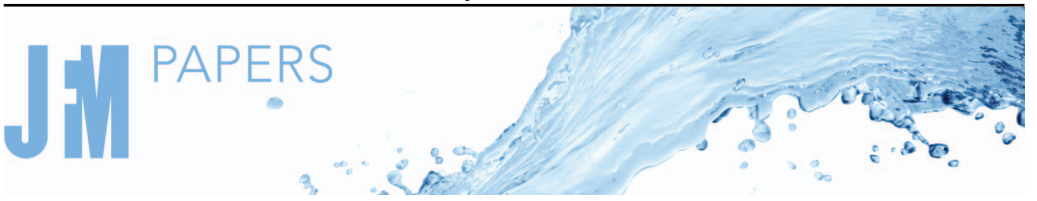
J. Fluid Mech. (2026), *vol.* 1033, A37, doi:10.1017/jfm.2026.11462



Electromagnetic flow control in hypersonic rarefied environment

Zhigang Pu[1] **and Kun Xu**[1,2]

[1]Department of Mathematics, Hong Kong University of Science and Technology, Clear Water Bay, Kowloon Hong Kong, PR China

[2]Shenzhen Research Institute, Hong Kong University of Science and Technology, Shenzhen, PR China

Corresponding author: Kun Xu, makxu@ust.hk

(Received 19 September 2025; revised 23 February 2026; accepted 20 March 2026)

The unified gas-kinetic wave-particle (UGKWP) method, developed for the multiscale simulation of partially ionised plasmas, is applied to model electromagnetic flows around a hemisphere spanning regimes from near-continuum to rarefied conditions. To the best of our knowledge, this study presents the first application of a multiscale plasma solver to such a problem. In the formulation, neutrals, ions and electrons are treated as distinct species. The numerical implementation is validated through comparisons with experimental data for a Mach 4.75 pre-ionised argon flow, where UGKWP results show close agreement with the experimental data. A further comparative study across different Knudsen numbers demonstrates that rarefaction effects weaken the influence of electromagnetic control. These findings highlight the capability of UGKWP in modelling electromagnetic control problems and underscore the significant role of rarefied effects in predicting flow-control behaviour, thereby emphasising the necessity of multiscale modelling in plasma flow applications.

Key words: hypersonic flow, rarefied gas flow

1. Introduction

Magnetohydrodynamic (MHD) thermal protection technology holds strategic significance for both national defence systems and deep-space exploration missions. During hypersonic flight, a strong externally applied magnetic field interacts with the weakly ionised gas produced by intense shock waves, increasing the shock standoff distance and thereby reducing the heat flux to the vehicle surface. The theoretical foundations of this technology

© The Author(s), 2026. Published by Cambridge University Press. This is an Open Access article, distributed under the terms of the Creative Commons Attribution licence (https://creativecommons.org/licenses/by/4.0/), which permits unrestricted re-use, distribution and reproduction, provided the original article is properly cited.

https://doi.org/10.1017/jfm.2026.11462 Published online by Cambridge University Press

date back to the 1950s US-Soviet space race, when Resler Jr & Sears (1958) pioneered the formulation of fundamental magneto-aerodynamic equations. They modelled weakly ionised plasma in high-speed, high-enthalpy flows as conducting fluids, incorporating Lorentz force and Joule heating terms into the modified Navier–Stokes equations.

Over subsequent decades, considerable progress was made in theoretical, computational and experimental aspects of MHD thermal protection. Bush (1958) provided an analytical solution describing the magnetic field's effect on shock standoff distance, while Ziemer & Bush (1958) later provided experimental validation using a Mach 4.5 sphere model, marking important early milestones. Cambel & Porter (1967) further investigated the Hall effect's detrimental impact on magnetic control efficiency and conducted corresponding experiments using pre-ionised argon gas, creating benchmark datasets that remain valuable for numerical validation. Following these foundational studies, advances in computational fluid dynamics enabled high-fidelity simulations of MHD flows (Poggie & Gaitonde 2002; Fujino, Yoshino & Ishikawa 2008; Kai, Jun & Weiqiang 2017). Recent numerical studies have increasingly incorporated complex physical phenomena, such as rarefied gas effects, and plasma sheath and wall interactions. For example, Fawley *et al.* (2022) used direct simulation Monte Carlo (DSMC) methods to model conductivity in transitional flow regimes, while Katsurayama *et al.* (2008) applied DSMC to simulate rarefied gas effects, approximating the Lorentz force as a body force rather than explicitly resolving charged particle trajectories. Jin, Peng & Feng (2025) investigated the rarefied MHD flow using the extended Navier–Stokes method, highlighting the significance of the rarefied gas effect in hypersonic MHD simulations in the near-continuum regime. Parent *et al.* (2023) further quantified the impact of plasma sheaths on the electron temperature.

Despite these advancements, most numerical simulations rely on MHD equations, whose applicability diminishes under high-altitude conditions characterised by large Knudsen numbers. In such regimes, the continuum assumption inherent to MHD-based models breaks down (Lani *et al.* 2023). DSMC-based approaches become computationally prohibitive due to the need for excessively dense meshes and small time steps, which are restricted by the mean free path scale (Boyd & Schwartzentruber 2017). Accurately capturing flow physics across continuum, transitional and rarefied regimes thus requires a genuinely multiscale numerical approach. Addressing these challenges, recent developments have led to the unified gas-kinetic wave-particle (UGKWP) method, which enables robust modelling of multiscale neutral gas flows from the rarefied to continuum regimes (Zhu *et al.* 2019; Liu, Zhu & Xu 2020). The UGKWP framework has since been systematically extended to a variety of transport phenomena, including plasma (Liu & Xu 2021; Pu, Liu & Xu 2024), granular flows (Yang *et al.* 2022, 2024), radiative transfer (Liu *et al.* 2023; Yang *et al.* 2025) and phonon transport (Liu *et al.* 2025), demonstrating its capability to capture non-equilibrium transport physics. Most recently, UGKWP has been specifically applied to partially ionised plasma flows (Pu & Xu 2025). In the continuum regime, UGKWP accurately recovers ideal MHD, dissipative MHD and multi-fluid models; as the flow transitions to rarefied conditions, the method seamlessly shifts to a particle-based description, effectively capturing kinetic plasma behaviour and recovering particle-in-cell (PIC) dynamics in the collisionless limit.

In this work, we apply the UGKWP method to modelling the electromagnetic control problems in the rarefied environments. The remainder of this paper is organised as follows: § 2 provides a concise overview of the UGKWP method for partially ionised plasma; § 3 presents the numerical test results; and § 4 offers the main conclusions of this study.

https://doi.org/10.1017/jfm.2026.11462 Published online by Cambridge University Press

2. UGKWP method

2.1. *Governing equations*

In this subsection, we introduce the physical models and governing equations used in this study. Theoretically, the Bhatnagar–Gross–Krook (BGK)–Maxwell system can be used to model the partially ionised plasma (Pu & Xu 2025),

$$\begin{aligned}
&\frac{\partial f_\alpha}{\partial t}+\boldsymbol{u}_\alpha\cdot\nabla_{\boldsymbol{x}} f_\alpha+\frac{q_\alpha(\boldsymbol{E}+\boldsymbol{u}_\alpha\times\boldsymbol{B})}{m_\alpha}\cdot\nabla_{\boldsymbol{u}} f_\alpha=Q_\alpha,\\
&\frac{\partial \boldsymbol{B}}{\partial t}+\nabla_{\boldsymbol{x}}\times\boldsymbol{E}=0,\quad \frac{\partial \boldsymbol{E}}{\partial t}-c^2\nabla_{\boldsymbol{x}}\times\boldsymbol{B}=-\frac{1}{\epsilon_0}\boldsymbol{J},\\
&\nabla_{\boldsymbol{x}}\cdot\boldsymbol{E}=\frac{\rho_c}{\epsilon_0},\quad \nabla_{\boldsymbol{x}}\cdot\boldsymbol{B}=0,
\end{aligned}\tag{2.1}$$

where $f_\alpha=f_\alpha(t,\boldsymbol{x},\boldsymbol{u})$ is the microscopic distribution function for species α ($\alpha=i$ for ion and $\alpha=e$ for electron, $\alpha=n$ for atom) at space and time $(\boldsymbol{x},t)$, and microscopic translational velocity $\boldsymbol{u}$; q_α is the charge carried by species α; $\boldsymbol{E}$, $\boldsymbol{B}$ is the electric and magnetic field strength; ϵ_0 is the permittivity of free space and c is the light speed; $\boldsymbol{J}$ is the electric current density; ρ_c is the electric charge density. Here, $Q_\alpha=\sum_{k\neq\alpha}Q_{\alpha k}(f_\alpha,f_k)$ is the collision operator of species α between species k, approximated by the Andries–Aoki–Perthame (AAP) model (Andries, Aoki & Perthame 2002),

$$Q_\alpha=\frac{g_\alpha^M-f_\alpha}{\tau_\alpha},\tag{2.2}$$

where g_α^M is a Maxwellian distribution,

$$g_\alpha^M=\rho_\alpha\left(\frac{m_\alpha}{2\pi k\bar{T}_\alpha}\right)^{3/2}\exp\left(-\frac{m_\alpha}{2k_B\bar{T}_\alpha}\left(\boldsymbol{u}_\alpha-\bar{\boldsymbol{U}}_\alpha\right)^2\right),\tag{2.3}$$

and post-collision velocity $\bar{\boldsymbol{U}}_\alpha$ and temperature $\bar{T}_\alpha$ are given as

$$\begin{aligned}
&\bar{\boldsymbol{U}}_\alpha=\boldsymbol{U}_\alpha+\frac{\tau_\alpha}{m_\alpha}\sum_{k=1}^{N}2\mu_{\alpha k}\chi_{\alpha k}n_k(\boldsymbol{U}_k-\boldsymbol{U}_\alpha),\\
&\bar{T}_\alpha=T_\alpha-\frac{m_\alpha}{3k_B}\left(\bar{\boldsymbol{U}}_\alpha-\boldsymbol{U}_\alpha\right)^2+\tau_\alpha\sum_{k=1}^{N}\frac{4\mu_{\alpha k}\chi_{\alpha k}n_k}{m_\alpha+m_k}\left(T_k-T_\alpha+\frac{m_k}{3k_B}(\boldsymbol{U}_k-\boldsymbol{U}_\alpha)^2\right),
\end{aligned}\tag{2.4}$$

where $\mu_{\alpha k}=m_\alpha m_k/(m_\alpha+m_k)$ is reduced mass, N is number of species in the system. Species α's mean relaxation time τ_α is determined by $1/\tau_\alpha=\sum_{k=1}^{m}\chi_{\alpha k}n_k$, and interaction coefficient $\chi_{\alpha k}$ for the variable hard sphere (VHS) model is (Morse 1963)

$$\chi_{\alpha k}=\frac{(5-2\omega)(7-2\omega)\sqrt{\pi}}{15}\left(\frac{2k_BT_\alpha}{m_\alpha}+\frac{2k_BT_k}{m_k}\right)^{1/2}\left(\frac{d_\alpha+d_k}{2}\right)^2,\tag{2.5}$$

where d_α, d_k are the diameters of the particles. The temperature modifies the molecular diameter as $(d/d_{ref})^2=(T/T_{ref})^{(1/2)-\omega}$, where ω is the power coefficient between viscosity and temperature (Bird 1976). Specific diameters for each species are presented in the subsequent numerical studies. For complex interactions involving neutral and charged species, experimentally derived fitted curves will be employed and presented in the numerical study section. The AAP model exhibits a Prandtl number of unity. Future work will extend the multi-relaxation-time, multi-species kinetic model to more accurately

https://doi.org/10.1017/jfm.2026.11462 Published online by Cambridge University Press

capture the simultaneous behaviour of viscosity and thermal conductivity, referencing work such as Bisi *et al.* (2022) and Li, Zeng & Wu (2024).

For hypersonic applications, the BGK–Maxwell system can be simplified. In many such applications, the ionised gas within the shock layer exhibits low electrical conductivity σ^{cond} (Poggie & Gaitonde 2002). This leads to a small induced current density $\boldsymbol{J}$ according to the Ohm's law $\boldsymbol{J} = \sigma^{cond}(\boldsymbol{E} + \boldsymbol{U} \times \boldsymbol{B})$. Consequently, the magnetic field produced by this current is significantly weaker than the externally applied magnetic field $\boldsymbol{B}_{ext}$. This allows for the neglect of magnetic field distortion by the flow field, enabling the assumption of a static magnetic field for the present investigation. Faraday's law can be neglected since the static magnetic field will generate no transverse electric field. Furthermore, the hyperbolic divergence cleaning technique realises the charge neutrality (Munz *et al.* 2000):

$$\epsilon_0 \frac{\partial \boldsymbol{E}}{\partial t} + c^2 \nabla \phi = -\boldsymbol{J}, \quad \frac{\partial \phi}{\partial t} + \nabla \cdot \boldsymbol{E} = \frac{\rho_c}{\epsilon_0}, \tag{2.6}$$

where ϕ is the artificial correction potential. An approximate Debye length of 10^{-4} m is implemented to alleviate numerical stiffness. Therefore, the final form of the physical model is given as

$$\begin{aligned} &\frac{\partial f_\alpha}{\partial t} + \boldsymbol{u}_\alpha \cdot \nabla_{\boldsymbol{x}} f_\alpha + \frac{q_\alpha(\boldsymbol{E} + \boldsymbol{u}_\alpha \times \boldsymbol{B}_{ext})}{m_\alpha} \cdot \nabla_{\boldsymbol{u}} f_\alpha = Q_\alpha, \\ &\epsilon_0 \frac{\partial \boldsymbol{E}}{\partial t} + c^2 \nabla \phi = -\boldsymbol{J}, \quad \frac{\partial \phi}{\partial t} + \nabla \cdot \boldsymbol{E} = \frac{\rho_c}{\epsilon_0}. \end{aligned} \tag{2.7}$$

In the fluid limit $\tau_\alpha \to 0$, (2.7) turns to a multi-fluid equation as

$$\begin{aligned} &\partial_t \rho_n + \nabla_{\boldsymbol{x}} \cdot (\rho_n \boldsymbol{U}_n) = 0, \\ &\partial_t (\rho_n \boldsymbol{U}_n) + \nabla_{\boldsymbol{x}} \cdot (\rho_n \boldsymbol{U}_n \boldsymbol{U}_n + p_n \mathbb{I}) = R_n, \\ &\partial_t \mathscr{E}_n + \nabla_{\boldsymbol{x}} \cdot ((\mathscr{E}_n + p_n) \boldsymbol{U}_n) = S_n, \\ &\partial_t \rho_i + \nabla_{\boldsymbol{x}} \cdot (\rho_i \boldsymbol{U}_i) = 0, \\ &\partial_t (\rho_i \boldsymbol{U}_i) + \nabla_{\boldsymbol{x}} \cdot (\rho_i \boldsymbol{U}_i \boldsymbol{U}_i + p_i \mathbb{I}) = q_i n_i (\boldsymbol{E} + \boldsymbol{U}_i \times \boldsymbol{B}_{ext}) + R_i, \\ &\partial_t \mathscr{E}_i + \nabla_{\boldsymbol{x}} \cdot ((\mathscr{E}_i + p_i) \boldsymbol{U}_i) = q_i n_i \boldsymbol{U}_i \cdot \boldsymbol{E} + S_i, \\ &\partial_t \rho_e + \nabla_{\boldsymbol{x}} \cdot (\rho_e \boldsymbol{U}_e) = 0, \\ &\partial_t (\rho_e \boldsymbol{U}_e) + \nabla_{\boldsymbol{x}} \cdot (\rho_e \boldsymbol{U}_e \boldsymbol{U}_e + p_e \mathbb{I}) = q_e n_e (\boldsymbol{E} + \boldsymbol{U}_e \times \boldsymbol{B}_{ext}) + R_e, \\ &\partial_t \mathscr{E}_e + \nabla_{\boldsymbol{x}} \cdot ((\mathscr{E}_e + p_e) \boldsymbol{U}_e) = q_e n_e \boldsymbol{U}_e \cdot \boldsymbol{E} + S_e, \\ &\epsilon_0 \frac{\partial \boldsymbol{E}}{\partial t} + c^2 \nabla \phi = -\boldsymbol{J}, \quad \frac{\partial \phi}{\partial t} + \nabla \cdot \boldsymbol{E} = \frac{\rho_c}{\epsilon_0}, \end{aligned} \tag{2.8}$$

where ρ_α, $\boldsymbol{U}_\alpha$, $\mathscr{E}_\alpha$ represent the mass density, macroscopic velocity and energy density of species α, and p_α is the thermal pressure of species α. Here, R_α, S_α are the source terms due to cross-species momentum and energy transfer. In the limit of a strong magnetic field, negligible electron mass and the non-relativistic regime, (2.7) simplifies to MHD equations. A detailed asymptotic analysis of this reduction is provided by Pu & Xu (2025).

2.2. *UGKWP method*

In this subsection, the UGKWP method to solve the system (2.7) as it transitions from the rarefied regime to the continuum regime is introduced. First, the multispecies collision operator is rewritten as

$$Q_\alpha = \frac{g_\alpha^{eq} - f_\alpha}{\tau_\alpha} + \frac{g_\alpha^{M} - g_\alpha^{eq}}{\tau_\alpha}, \tag{2.9}$$

https://doi.org/10.1017/jfm.2026.11462 Published online by Cambridge University Press

where g_α^{eq} is the Maxwellian distribution by collision within the same species and g_α^M is the Maxwellian distribution after collisions between different species. Then, the operator splitting method is used to solve system (2.7) and (2.9) with time step Δt,

$$\mathcal{L}_1 : \frac{\partial f_\alpha}{\partial t} + \boldsymbol{u}_\alpha \cdot \nabla_{\boldsymbol{x}} f_\alpha = \frac{g_\alpha^{eq} - f_\alpha}{\tau_\alpha}, \tag{2.10}$$

$$\mathcal{L}_2 : \frac{\partial f_\alpha}{\partial t} + \frac{q_\alpha(\boldsymbol{E} + \boldsymbol{u}_\alpha \times \boldsymbol{B}_{ext})}{m_\alpha} \cdot \nabla_{\boldsymbol{u}} f_\alpha = 0, \quad \epsilon_0 \frac{\partial \boldsymbol{E}}{\partial t} = -\boldsymbol{J}, \tag{2.11}$$

$$\mathcal{L}_3 : \frac{\partial f_\alpha}{\partial t} = \frac{g_\alpha^M - g_\alpha^{eq}}{\tau_\alpha}, \tag{2.12}$$

$$\mathcal{L}_4 : \epsilon_0 \frac{\partial \boldsymbol{E}}{\partial t} + c^2 \nabla \phi = 0, \quad \frac{\partial \phi}{\partial t} + \nabla \cdot \boldsymbol{E} = \frac{\rho_c}{\epsilon_0}. \tag{2.13}$$

The variables after each update are denoted as

$$\begin{aligned} &\mathcal{L}_1 : f_\alpha^n \to f_\alpha^*, \boldsymbol{W}_\alpha^n \to \boldsymbol{W}_\alpha^*, \qquad \mathcal{L}_2 : f_\alpha^* \to f_\alpha^{**}, \boldsymbol{W}_\alpha^* \to \boldsymbol{W}_\alpha^{**}, \boldsymbol{E}^n \to \boldsymbol{E}^*, \\ &\mathcal{L}_3 : f_\alpha^{**} \to f_\alpha^{n+1}, \boldsymbol{W}_\alpha^{**} \to \boldsymbol{W}_\alpha^{n+1}, \ \mathcal{L}_4 : \boldsymbol{E}^* \to \boldsymbol{E}^{n+1}, \phi^n \to \phi^{n+1}, \end{aligned} \tag{2.14}$$

where $\boldsymbol{W}_\alpha = (\rho_\alpha, \rho_\alpha \boldsymbol{U}_\alpha, \rho_\alpha \mathscr{E}_\alpha)$ is mass, momentum and energy densities of species α.

First, we introduce algorithms for solving $\mathcal{L}_1$. For simplicity, the species subscript α is omitted here. The BGK equation without the force term is written as

$$\frac{\partial f}{\partial t} + \boldsymbol{u} \cdot \nabla_x f = \frac{g - f}{\tau}, \tag{2.15}$$

the time-dependent solution of the distribution function at the interface can be written as

$$f\ (\boldsymbol{x}, \boldsymbol{u}, \boldsymbol{\xi}, t) = \frac{1}{\tau} \int_0^t g(\boldsymbol{x}', \boldsymbol{u}, \boldsymbol{\xi}, t') e^{-(t-t')/\tau}\, \mathrm{d}t' + e^{-t/\tau} f_0\ (\boldsymbol{x} - \boldsymbol{u}t)\ , \tag{2.16}$$

where τ is the local mean relaxation time, f_0 is the initial gas distribution function at $t = 0$ and g is equilibrium distribution along the characteristic line $\boldsymbol{x}' = \boldsymbol{x} - \boldsymbol{u}t'$. Expanding the equilibrium distribution function by the Taylor series to the second-order accuracy,

$$g' = g + \boldsymbol{g}_x \cdot (\boldsymbol{x}' - \boldsymbol{x}) + g_t (t' - t), \tag{2.17}$$

where $g \equiv g(\boldsymbol{x}, \boldsymbol{u}, \boldsymbol{\xi}, t)$, $g' \equiv g(\boldsymbol{x}', \boldsymbol{u}, \boldsymbol{\xi}, t')$. By substituting them into (2.16), the numerical multiscale evolution solution for simulation particles can be obtained,

$$f(\boldsymbol{x}, \boldsymbol{u}, \boldsymbol{\xi}, t) = \left(1 - e^{-t/\tau}\right) g^+(\boldsymbol{x}, \boldsymbol{u}, \boldsymbol{\xi}, t) + e^{-t/\tau} f_0\ (\boldsymbol{x} - \boldsymbol{u}t)\ , \tag{2.18}$$

where

$$g^+ = g + \left(\frac{te^{-t/\tau}}{1 - e^{-t/\tau}} - \tau\right) \boldsymbol{u} \cdot \boldsymbol{g}_x + \left(\frac{t}{1 - e^{-t/\tau}} - \tau\right) g_t. \tag{2.19}$$

Equation (2.19) describes the solution to the BGK equation, where the distribution function f at time t is a combination of the initial distribution function f_0 and the Taylor expansion of the equilibrium state g. From the particles' perspective, this equation implies that a particle has a probability of $e^{-t/\tau}$ to freely stream during the time interval $[0, t]$, and a probability of $(1 - e^{-t/\tau})$ to collide with other particles. After multiple collisions, the particle distribution will reach the equilibrium state g^+, whose degree of freedom can be degenerated.

Based on this physical picture, the UGKWP method represents the velocity distribution function in a micro–macro coupled way. A portion of the distribution is captured

https://doi.org/10.1017/jfm.2026.11462 Published online by Cambridge University Press

analytically through the equilibrium distribution function g^+, while the remaining part is represented by stochastic simulation particles $P_k = (m_k, \boldsymbol{x}_k, \boldsymbol{u}_k)$. Here, m_k denotes the mass of simulation particle P_k, which corresponds to a cluster of real gas particles of the same species, and $\boldsymbol{x}_k$ and $\boldsymbol{u}_k$ represent the position and velocity of the simulation particle P_k, respectively.

According to (2.18), the cumulative distribution function of the particle's free streaming time t_f before the collision is given as

$$F(t_f < t) = \exp(-t/\tau), \tag{2.20}$$

from which the free stream time t_f can be sampled as $t_f = -\tau \ln(\eta)$ with η a random varible subject to the uniform distribution $\eta \sim U(0, 1)$. For a time step Δt, the particles with $t_f \geqslant \Delta t$ will undergo collisionless free streaming and the particles with $t_f < \Delta t$ will experience collisional interactions. The procedure of updating particles in the UGKWP method is as follows.

Step 1. During the time step, stream each particle P_k for a time period of $\min(\Delta t, t_{f,k})$. Then, identify and retain the collisionless particles, while removing the collisional particles. Calculate the free-transport flux across cell interfaces contributed by the particles and accumulate the total conservative quantities of the particles $\boldsymbol{W}_i^p$.

Step 2. After updating the macroscopic conservative variables, calculate the total conservative quantities of the collisional particles $\boldsymbol{W}_i^h$ from the updated conservative quantities $\boldsymbol{W}_i$ as $\boldsymbol{W}_i^h = \boldsymbol{W}_i - \boldsymbol{W}_i^p$.

Step 3. At the end of the time step, rebuild the velocity distribution. Calculate the analytical distribution $g^{+,c}$ and resample the collisionless particles from the distribution $g^{+,f}$ according to the updated conservative quantities, and sample the free-streaming time $t_{f,k}$ for each particle P_k from the cumulative distribution function $F(t_f < t) = \exp(-t/\tau)\ \boldsymbol{W}_i^h$.

Refer to Pu & Xu (2025) for a more detailed description of the procedure. In the procedure already outlined, the algorithm for updating the macroscopic conservative variables is introduced in the following paragraph. The evolution of the microscopic velocity distribution is now solved numerically using particles.

Based on the finite volume framework, the cell-averaged macroscopic conservative variables on a physical cell Ω_i are updated by the numerical flux through cell interfaces:

$$(\boldsymbol{W}_\alpha)_i^{n+1} = (\boldsymbol{W}_\alpha)_i^n - \frac{\Delta t}{|\Omega_i|} \sum_{s \in \partial \Omega_i} |l_s| (\mathscr{F}_{\boldsymbol{W}_\alpha})_s, \tag{2.21}$$

where $l_s \in \partial \Omega_i$ is the cell interface with centre $\boldsymbol{x}_s$ and outer unit normal vector $\boldsymbol{n}_s$; $|l_s|$ is the area of the cell interface. The numerical flux across interface $(\mathscr{F}_{\boldsymbol{W}_\alpha})_s$ can be evaluated from distribution function at the interface,

$$(\mathscr{F}_{\boldsymbol{W}_\alpha})_s = \frac{1}{\Delta t} \int_{t^n}^{t^{n+1}} \boldsymbol{u} \cdot \boldsymbol{n}_s f_\alpha(\boldsymbol{x}_s, \boldsymbol{u}, \boldsymbol{\xi}, t) \boldsymbol{\Psi} \mathrm{d}\boldsymbol{\Xi} \mathrm{d}t, \tag{2.22}$$

where $\boldsymbol{\Psi} = (1, \boldsymbol{u}, (1/2)(\boldsymbol{u}^2 + \boldsymbol{\xi}^2))$ is the conservative moments of distribution functions and $\mathrm{d}\boldsymbol{\Xi} = \mathrm{d}\boldsymbol{u}\, d\boldsymbol{\xi}$ is the volume element in the phase space. For the cell interface l_s, the distribution function $f_\alpha(\boldsymbol{x}_s, \boldsymbol{u}, \boldsymbol{\xi}, t)$ cannot be analytically represented in the transitional and collisionless regimes, thus requiring direct tracking of its evolution as introduced in the previous paragraph. This numerical flux of the macroscopic conservative variable can be

https://doi.org/10.1017/jfm.2026.11462 Published online by Cambridge University Press

split into the equilibrium flux and free streaming flux according to (2.16). The equilibrium flux is

$$(\mathscr{F}_{\boldsymbol{W}})_s^g = \frac{1}{\Delta t}\int_{t^n}^{t^{n+1}} \boldsymbol{u}\cdot\boldsymbol{n}_s \left[\frac{1}{\tau}\int_0^t g(\boldsymbol{x}', \boldsymbol{u}, \boldsymbol{\xi}, t')e^{-(t-t')/\tau}\mathrm{d}t'\right]\boldsymbol{\Psi}\,\mathrm{d}\boldsymbol{\Xi}\,\mathrm{d}t \tag{2.23}$$

and the free streaming flux is

$$(\mathscr{F}_{\boldsymbol{W}})_s^f = \frac{1}{\Delta t}\int_{t^n}^{t^{n+1}} \boldsymbol{u}\cdot\boldsymbol{n}_s \left[e^{-t/\tau} f_0\left(\boldsymbol{x}-\boldsymbol{u}t\right)\right]\boldsymbol{\Psi}\,\mathrm{d}\boldsymbol{\Xi}\,\mathrm{d}t. \tag{2.24}$$

The equilibrium flux can be calculated directly from the macroscopic conservative variables. Assume in (2.22), $\boldsymbol{x}_s = \boldsymbol{0}$ and $t^n = 0$, the equilibrium g at the cell interface is obtained by conservation constraint

$$\int g\boldsymbol{\Psi}\,\mathrm{d}\boldsymbol{\Xi} = \int_{\boldsymbol{u}\cdot\boldsymbol{n}>0} g^l\boldsymbol{\Psi}\,\mathrm{d}\boldsymbol{\Xi} + \int_{\boldsymbol{u}\cdot\boldsymbol{n}<0} g^r\boldsymbol{\Psi}\,\mathrm{d}\boldsymbol{\Xi}. \tag{2.25}$$

The spatial and time derivatives can be obtained,

$$\int g_x\boldsymbol{\Psi}\,\mathrm{d}\boldsymbol{\Xi} = \boldsymbol{W}_x, \quad \int g_t\boldsymbol{\Psi}\,\mathrm{d}\boldsymbol{\Xi} = -\int \boldsymbol{u}\cdot g_x\boldsymbol{\Psi}\,\mathrm{d}\boldsymbol{\Xi}, \tag{2.26}$$

where g^l and g^r are the equilibrium distributions according to the reconstructed left and right side conservative variables at cell interface $\boldsymbol{W}^l$, $\boldsymbol{W}^r$, and $\boldsymbol{W}_x$ is the reconstructed spatial derivative of conservative variables at cell interface. The van Leer limiter is used to achieve a second-order accuracy in space reconstruction. In regions with strong gradients, the limiter restricts the gradient to prevent unphysical oscillations. Substituting the reconstructed equilibrium distribution into the equilibrium flux, we have

$$(\mathscr{F}_{\boldsymbol{W}})_s^g = \int \boldsymbol{u}\cdot\boldsymbol{n}_s\left(C_1 g_0 + C_2\boldsymbol{u}\cdot\boldsymbol{g}_{0x} + C_3 g_{0t}\right)\Psi\,\mathrm{d}\boldsymbol{\Xi}, \tag{2.27}$$

where the time integration coefficients are

$$C_1 = \Delta t - \tau\left(1-e^{-\Delta t/\tau}\right), \tag{2.28}$$

$$C_2 = 2\tau^2\left(1-e^{-\Delta t/\tau}\right) - \tau\Delta t - \tau\Delta t e^{-\Delta t/\tau}, \tag{2.29}$$

$$C_3 = \frac{\Delta t^2}{2} - \tau\Delta t + \tau^2\left(1-e^{\Delta t/\tau}\right). \tag{2.30}$$

Next, we consider the free stream flux $(\mathscr{F}_{\boldsymbol{W}})_s^f$. As stated in the last subsection, the initial distribution is represented partially by an analytical distribution $g_a^{+,c}$ and partially by particles, and therefore, the free stream flux is also calculated partially from the reconstructed analytical distribution as $(\mathscr{F}_{\boldsymbol{W}})_s^{f,w}$ and partially from particles as $(\mathscr{F}_{\boldsymbol{W}})_s^{f,p}$. The initial analytical distribution $g_\alpha^{+,c}$ is reconstructed as

$$g_0^{+,c}(\boldsymbol{x}, \boldsymbol{u}) = g_0^{+,c} + \boldsymbol{g}_{0x}^{+,c}\cdot\boldsymbol{x}, \tag{2.31}$$

which gives

$$(\mathscr{F}_{\boldsymbol{W}})_s^{f,w} = \int \boldsymbol{u}\cdot\boldsymbol{n}_s\left(C_4 g_0^{+,c} + C_5\boldsymbol{u}\cdot g_{0x}^{+,c}\right)\boldsymbol{\Psi}\,\mathrm{d}\boldsymbol{\Xi}, \tag{2.32}$$

where the time integration coefficients are

https://doi.org/10.1017/jfm.2026.11462 Published online by Cambridge University Press

$$C_4 = \tau\left(1 - e^{-\Delta t/\tau}\right) - \Delta t e^{-\Delta t/\tau}, \tag{2.33}$$

$$C_5 = \tau\,\Delta t e^{-\Delta t/\tau} - \tau^2\left(1 - e^{-\Delta t/\tau}\right) + \frac{\Delta t^2}{2} e^{-\Delta t/\tau}. \tag{2.34}$$

The net particle flux $(\mathscr{F}_{\boldsymbol{W}})_s^{f,p}$ is calculated as

$$(\mathscr{F}_{\boldsymbol{W}})_s^{f,p} = \sum_{k \in P_{\partial\Omega_i^+}} \boldsymbol{W}_{P_k} - \sum_{k \in P_{\partial\Omega_i^-}} \boldsymbol{W}_{P_k}, \tag{2.35}$$

where $\boldsymbol{W}_{P_k} = (m_k, m_k \boldsymbol{v}_k, (1/2) m_k \boldsymbol{v}_{\boldsymbol{k}}^2)$, $P_{\partial\Omega_i^-}$ is the index set of the particles streaming out of cell Ω_i during a time step and $P_{\partial\Omega_i^+}$ is the index set of the particles streaming into cell Ω_i. Finally, the update formula for conservative variables is

$$\boldsymbol{W}_{\boldsymbol{i}}^* = \boldsymbol{W}_{\boldsymbol{i}}^{\boldsymbol{n}} - \sum_s \frac{\Delta t}{|\Omega_i|} |l_s| (\mathscr{F}_{\boldsymbol{W}})_s^g - \sum_s \frac{\Delta t}{|\Omega_i|} |l_s| (\mathscr{F}_{\boldsymbol{W}})_s^{f,w} + \frac{1}{|\Omega_i|} (\mathscr{F}_{\boldsymbol{W}})_s^{f,p}. \tag{2.36}$$

The evolution of the macroscopic conservative variables due to species transport and diffusion has been solved by the coupled evolution of the microscopic particle transport and macroscopic fluid dynamics.

Subsequently, we solve the $\mathcal{L}_2$. The moment equation of (2.11) is first solved implicitly. Particles are then accelerated using the updated $\boldsymbol{E}^*$. Further details regarding the moment equation and the implicit linear system can be found from Pu & Xu (2025). Next, we solve $\mathcal{L}_3$; the moment equation of (2.12) is a set of nonlinear ordinary equations:

$$\frac{\partial \boldsymbol{U}_\alpha}{\partial t} = \frac{1}{m_\alpha} \sum_{k=1}^{N} 2\mu_{\alpha k} \chi_{\alpha k} n_k (\boldsymbol{U}_k - \boldsymbol{U}_\alpha), \tag{2.37}$$

$$\frac{\partial E_\alpha}{\partial t} = \sum_{k=1}^{N} \frac{2 m_k \chi_{\alpha k} n_k}{m_\alpha + m_k} \boldsymbol{U}_\alpha (\boldsymbol{U}_k - \boldsymbol{U}_\alpha) + \frac{3 k_B}{2 m_\alpha} \sum_{k=1}^{N} \frac{4 \mu_{\alpha k} \chi_{\alpha k} n_k}{m_\alpha + m_k} \left(T_k - T_\alpha + \frac{m_k}{3 k_B} (\boldsymbol{U}_k - \boldsymbol{U}_\alpha)^2 \right). \tag{2.38}$$

Discretise with the backward Euler scheme and solve it with the Newton iteration solver. The details are in Appendix B. Finally, in $\mathcal{L}_4$, (2.13) is solved by the flux vector splitting method. The overall algorithm flow chart is shown in figure 1.

In contrast to DSMC and PIC methods, the present approach circumvents the restrictive stability conditions tied to mesh size, and time step being smaller than the mean free path and mean collision time, respectively. For accurate physical resolution, a spatial grid size Δx of approximately $\sqrt{\lambda}$ is required, where λ denotes the mean free path (Guo, Li & Xu 2023). This relaxation of mesh constraints, especially in near-continuum regimes with small λ, leads to a substantial increase in computational efficiency compared with conventional particle methods.

3. Numerical studies

In this section, we conduct a three-dimensional simulation of Mach 4.75 argon flow around a hemisphere, replicating the experimental conditions reported by Cambel (1967). The UGKWP method employed here has been verified and validated against benchmark and practical rarefied and plasma problems extensively (Zhu *et al.* 2019; Liu *et al.* 2020; Liu & Xu 2021; Wei *et al.* 2023; Long, Wei & Xu 2024; Pu & Xu 2025; Cao *et al.* 2026).

https://doi.org/10.1017/jfm.2026.11462 Published online by Cambridge University Press

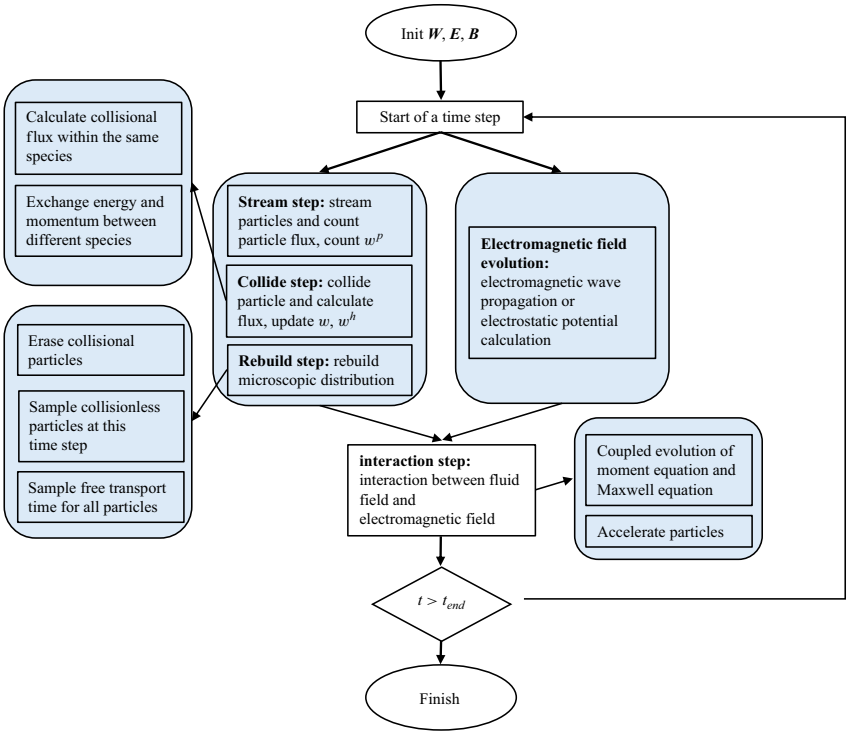


Figure 1. Flow chart of UGKWP method.

To further verify the code's accuracy in hypersonic plasma problems, we first compare the results with the experiment's results. Then, we change the Knudsen number of argon atoms to see how the control effects vary in different rarefied degrees.

3.1. *Validation against experiments*

The simulation imposes a hypersonic freestream flow in the $-x$ direction incident upon the hemisphere, as shown in figure 2(*a*). The hemisphere radius $r_n = 0.01905$ m. Here, 1/4 of the hemisphere is simulated, as shown in figure 2(*b*). The height of the first layer is 0.00005 m and the total cell number is 7488. A grid independence study is conducted, employing five mesh resolutions characterised by first-layer heights of $h = 0.0004$, 0.0002, 0.0001, 0.00005 and 0.000025 m. Relative to the hemispherical body diameter ($D \approx 0.04$ m), these correspond to h/D ratios of approximately 0.01, 0.005, 0.0025, 0.00125 and 0.000625, respectively. The resulting surface pressure and heat flux distributions of argon atom for each mesh are compared in figure 3. The surface pressure distribution (panel *a*) remains nearly invariant across all mesh resolutions, demonstrating rapid convergence. In contrast, the surface heat flux (panel *b*) exhibits greater sensitivity to grid refinement, gradually decreasing with finer meshes until converging. The results for $h = 0.00005$ m and $h = 0.000025$ m are essentially identical, confirming mesh independence. Based on this analysis, all subsequent simulations employ the mesh with $h = 0.00005$ m.

In the experiments, the inflow comprised a partially ionised argon flow generated by a plasma torch. Cambel (1967) estimated the ionisation degree to be $\alpha = 0.025$, and then Bisek, Boyd & Poggie (2010), employing a more refined Saha equation for weakly ionised atomic gases, re-estimated the ionisation degree as $\alpha = 0.00623$. This revised value is adopted in the present study. Cambel (1967) asserted that the flow remained chemically

https://doi.org/10.1017/jfm.2026.11462 Published online by Cambridge University Press

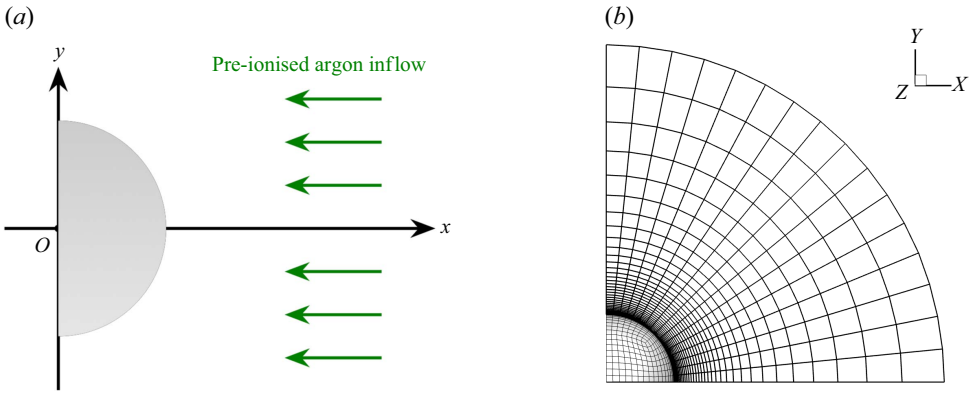


Figure 2. Computational domain specifications for hypersonic flow over a hemisphere: (*a*) case setting; (*b*) mesh setting.

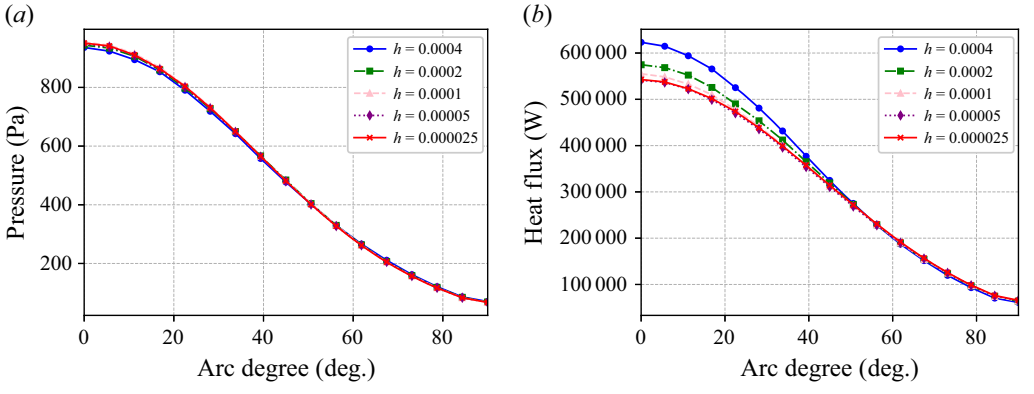


Figure 3. Distribution of surface pressure and heat flux in different mesh sizes: (*a*) surface pressure; (*b*) surface heat flux.

frozen, allowing the ionisation degree to be treated as a constant throughout the flow field. Detailed parameters are listed in table 1.

A magnetic dipole, with its magnetic moment oriented along the x-axis, is positioned at the centre of the hemisphere. Its orientation opposes the incoming flow along the stagnation line. The magnetic field generated by this dipole is defined as

$$\boldsymbol{B} = \frac{B_{max}}{2\left(\hat{x}^2+\hat{y}^2+\hat{z}^2\right)^{5/2}}\begin{bmatrix} 2\hat{x}^2-\left(\hat{y}^2+\hat{z}^2\right) \\ 3\hat{x}\hat{y} \\ 3\hat{x}\hat{z} \end{bmatrix}, \tag{3.1}$$

where $\hat{x}=x/r_n$, $\hat{y}=y/r_n$ and $\hat{z}=z/r_n$ represent the coordinates normalised by the hemisphere radius, r_n. The parameter B_{max} denotes the maximum magnetic field strength, which is attained at the stagnation point. Figure 4 displays the magnetic field lines of the dipole field in panel (*a*) and the magnitude in panel (*b*). In the following analysis, we employ B_{max} to characterise the magnetic field strength. Simulations are performed at four distinct magnetic field strengths: 0.223 T, 0.316 T, 0.387 T and 0.447 T.

In this case, the Ar–Ar, Ar^+–Ar^+, e^-–e^- collision is modelled as a VHS collision with $\omega=0.81$ and $d=4.17\times10^{-10}$ m. For charged–charged interactions (Ar^+–Ar^+ and

https://doi.org/10.1017/jfm.2026.11462 Published online by Cambridge University Press

Parameter	Value
Mach number	4.75
Knudsen number	0.044
Argon atomic mass	6.63×10^{-26} kg
Argon diameter (VHS)	4.17×10^{-10} m
Incoming argon density	1.09×10^{-4} kg m^{-1}
Incoming argon ion density	6.85×10^{-7} kg m^{-1}
Incoming electron number density	1.0332×10^{19} m^{-3}
Mass ratio m_{Ar^+}/m_{e^-}	10
Characteristic temperature	1100 K
Incoming electron temperature	5000 K
Wall temperature	1100 K
Incoming argon velocity	3000 m s^{-1}
Hemisphere radius	0.01905 m

Table 1. Simulation parameters for the rarefied argon flow around a hemisphere.

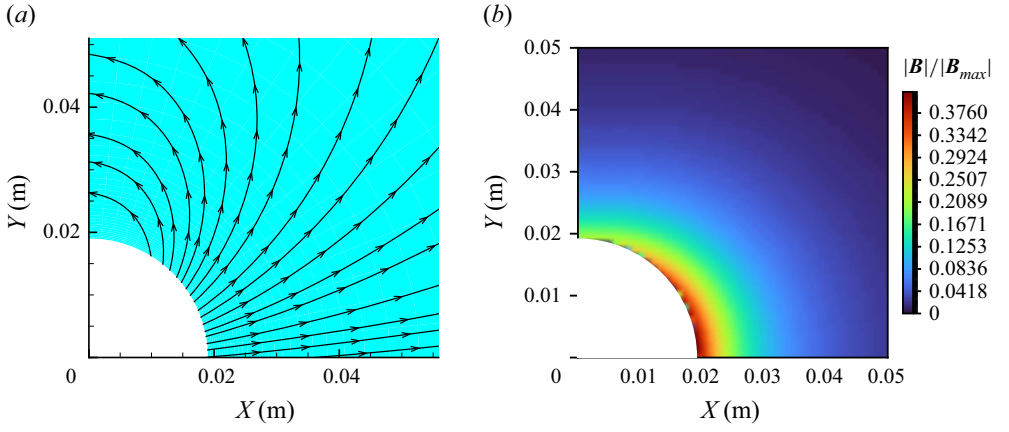


Figure 4. (*a*) Magnetic field lines and (*b*) magnetic field setting $|\boldsymbol{B}|/|\boldsymbol{B}_{max}|$.

$e^- - e^-$), Coulomb forces are, in principle, dominant. However, in the weakly ionised regime considered here ($n_e/n_{Ar} \ll 1$), such collisions occur infrequently compared with neutral-related collisions. Therefore, using the VHS model to approximate these two interactions introduces only a minor error, which is acceptable for the present plasma conditions. For the mixed species collisions Ar–Ar^+, Ar–e^-, Ar^+–e^-, cross-sections are described by fitted curves from Devoto (1973), as shown in table 2, for complex scattering mechanisms such as polarisation and charge-exchange effects that are not captured by simplified collision models. Electron mass was artificially increased ($m_{Ar^+}/m_{e^-} = 10$) to be computationally tractable. This modification, however, reduces the electrical conductivity. Therefore, the magnetic field magnitude is artificially increased, following the scaling by the similarity parameter $S = \sigma^{cond}|\boldsymbol{B}_0|^2 L_0/\rho_0|\boldsymbol{U}_0|$, see more explanation in Appendix A. Sensitivity experiments are performed for mass ratios from 10 to 40 at a fixed magnetic field strength of $B_{max} = 0.223$ T. As shown in figure 5, the number density profile of Ar exhibits only minor variations across the range considered, supporting the validity of this approach. To access the convergence status of simulations, we monitor the temporal evolution of averaged key surface quantities, specifically pressure and heat

https://doi.org/10.1017/jfm.2026.11462 Published online by Cambridge University Press

Collision pair	Fitted curve
$Ar - Ar^+$	$-0.00182T_{Ar^+} + 116.1$
$Ar - e^-$	$0.0004T_{e^-} - 0.3838$
$Ar^+ - e^-$	0.001

Table 2. Cross-section of Ar–Ar^+, Ar–e^-, Ar^+–e^- (unit is Å^2).

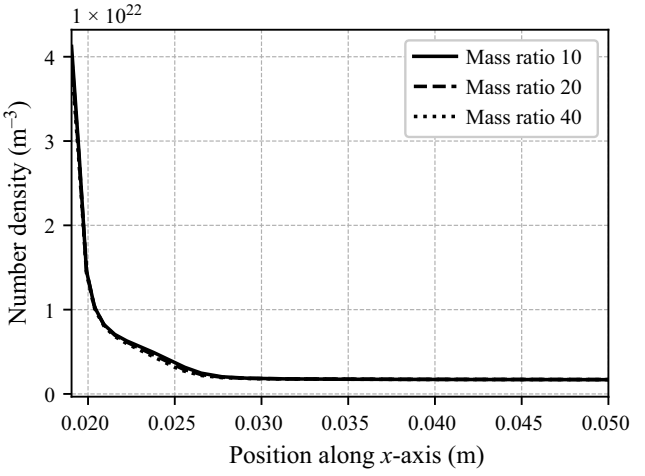


Figure 5. Comparision of the number density profile of Ar in the different mass ratios ($B_{max} = 0.223T$).

flux. The simulation is considered converged when these monitored quantities stabilise, indicating the absence of significant change.

Current formulation allows for the observation of distinct behaviours among atoms, ions and electrons, including velocity and temperature slip arising from rarefied effects. Figures 6 and 7 display contour distributions, with upper halves showing simulations without an external magnetic field and lower halves depicting results with background magnetic field strengths ($B_{max} = 0.447$ T). The data confirm that an applied magnetic field enhances shock standoff distance.

Figures 6(b) and 6(c) demonstrate that after the application of a magnetic field, both ions and electrons are significantly trapped near the stagnation point. The corresponding number density profiles of ions and electrons along the stagnation line are shown in figure 8(a). These profiles clearly indicate an increase in number density for both species following the application of the magnetic field. This increase occurs because the strong magnetic field in this stagnation region substantially suppresses transverse particle motion compared with the field-free condition. Consequently, charged particles are transported more directly to the wall, elevating the local number density. In contrast, within the shoulder region (the shoulder region comprises arc degrees spanning from approximately 30° to 60°, with the stagnation line serving as the 0° reference), the Lorentz force exerts a greater influence, deflecting charged particles away from the wall and resulting in a lower number density relative to the non-magnetic case, as evidenced in figures 6(b) and 6(c). The collision coupling between these charged particles and argon atoms then contributes to a slight accumulation of argon atoms in the stagnation region, as depicted in figure 6(a). Figures 6(d), 6(e) and 6(f) present the x-velocity of Ar, Ar^+ and e^-. In the stagnation

https://doi.org/10.1017/jfm.2026.11462 Published online by Cambridge University Press

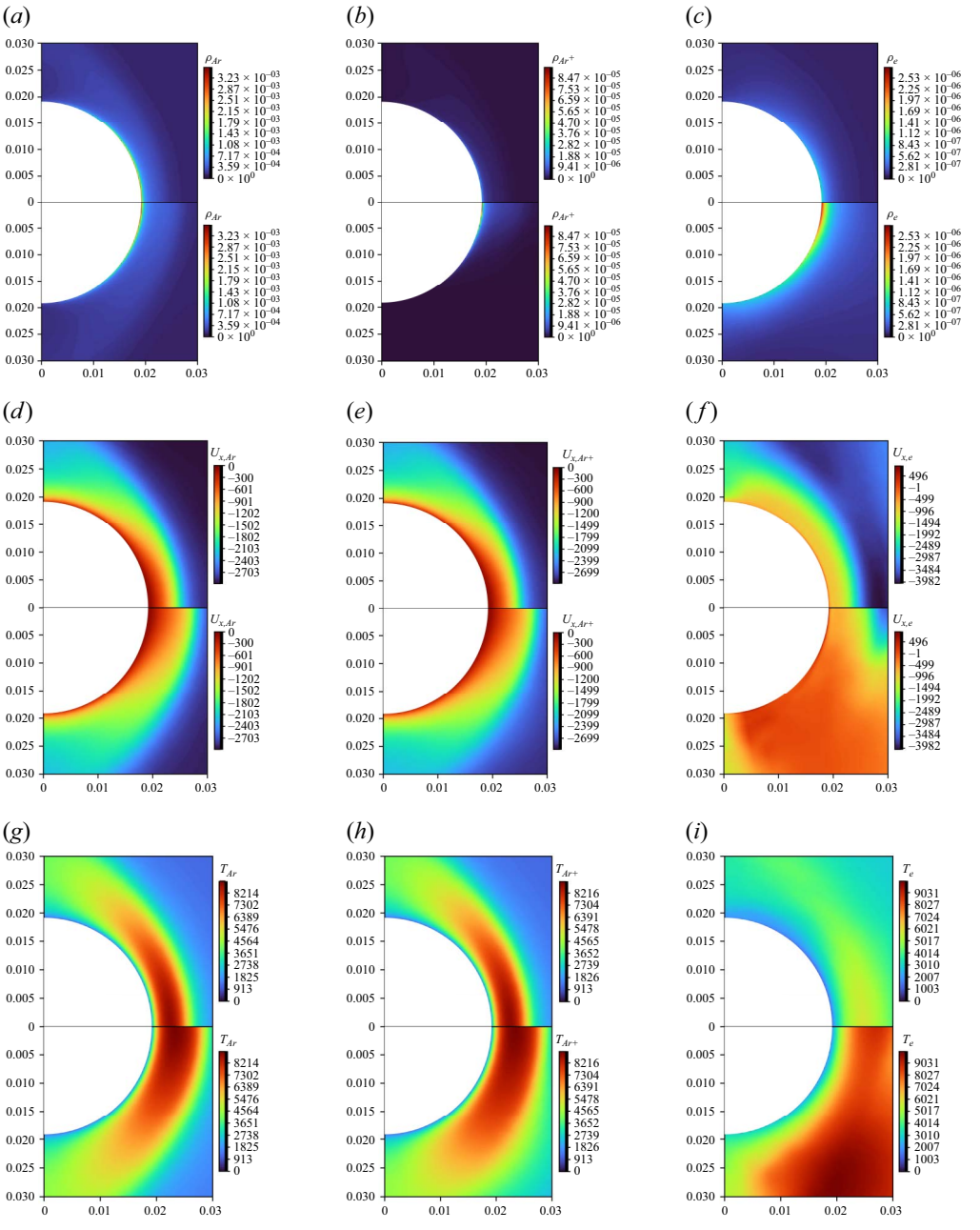


Figure 6. Contour plots without external magnetic field (upper) and with external magnetic field (lower) in the figures, where the first row is the mass density of (*a*) Ar, (*b*) Ar^+, (*c*) e^-; the second row is the x-velocity of (*d*) Ar, (*e*) Ar^+, (*f*) e^-; and third row is the temperature of (*g*) Ar, (*h*) Ar^+, (*i*) e^- at $B_{max} = 0.447$ T.

region, Ar^+ velocity closely follows Ar velocity. In the shoulder region, outside of shock, their velocities diverge due to the magnetic field influence on Ar^+. Electron velocity deviates significantly from heavy particles as the magnetic field more easily accelerates them and the velocity decoupling is further promoted by low collision frequencies in rarefied environments. Figures 6(*g*) to 6(*i*) show similar decoupling in temperature.

https://doi.org/10.1017/jfm.2026.11462 Published online by Cambridge University Press

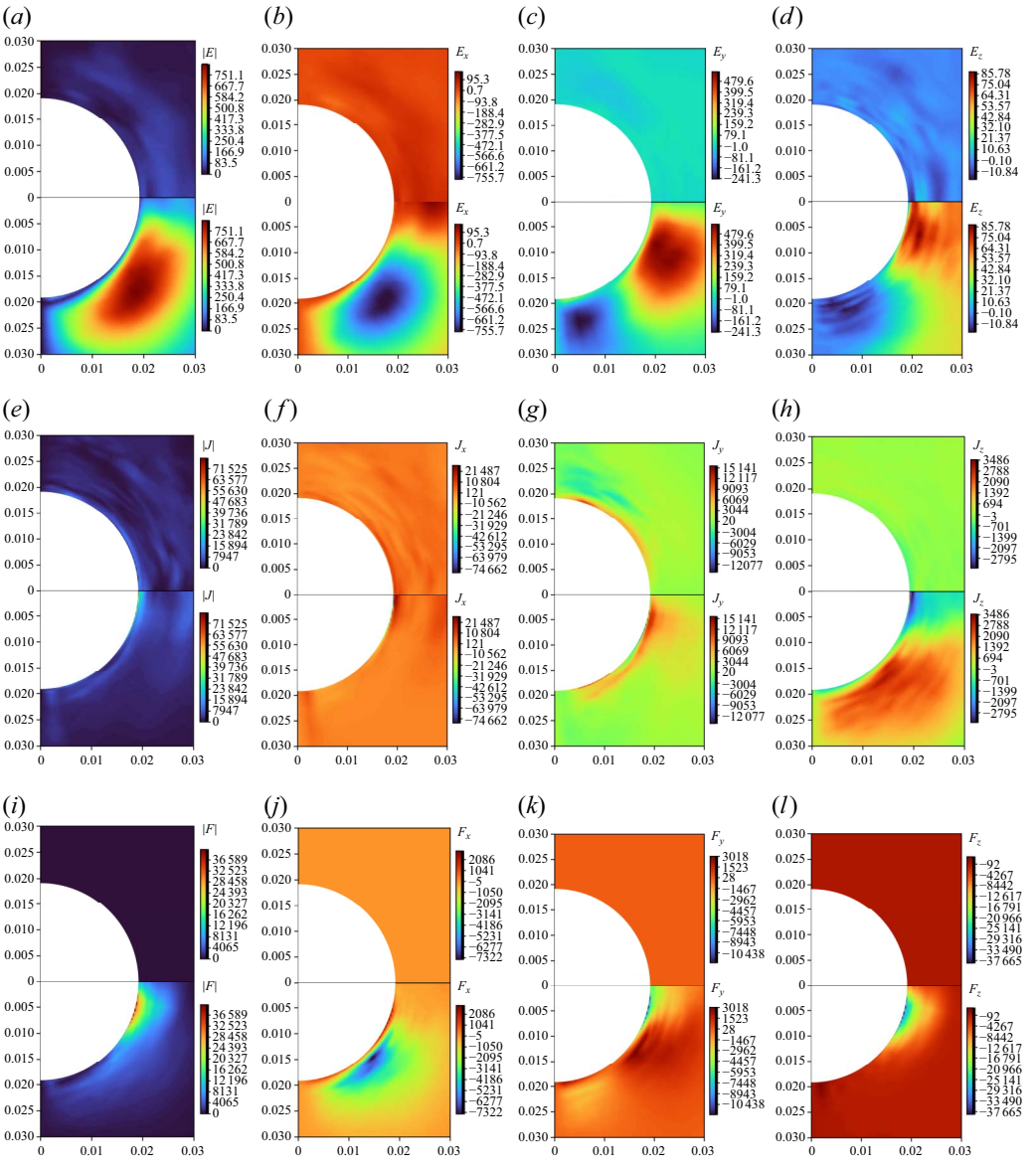


Figure 7. Contour plots of (*a*)–(*d*) electric field magnitude $|\boldsymbol{E}|$ and E_x, E_y, E_z, (*e*)–(*h*) current density magnitude $\boldsymbol{J}$ and J_x, J_y, J_z, (*i*)–(*l*) Lorentz force magnitude $|\boldsymbol{F}|$ and F_x, F_y, F_z at $B_{max} = 0.447$ T. Upper and lower figures refer to the results without and with external magnetic fields.

The present formulation also permits the observation of electric fields generated by diverse mechanisms. Figures 7(*a*) depict the electric field magnitude with and without an external magnetic field. In the absence of a magnetic field, the electric field remains generally weak, with localised peaks arising near the walls from sheath formation and across the shock front. Near the wall, the ion density exceeds the electron density, producing a net positive charge that establishes an electric field directed away from the wall to repel incoming ions. Across the shock front, the strong pressure gradient causes charge separation between ions and electrons. Applying a magnetic field alters this

https://doi.org/10.1017/jfm.2026.11462 Published online by Cambridge University Press

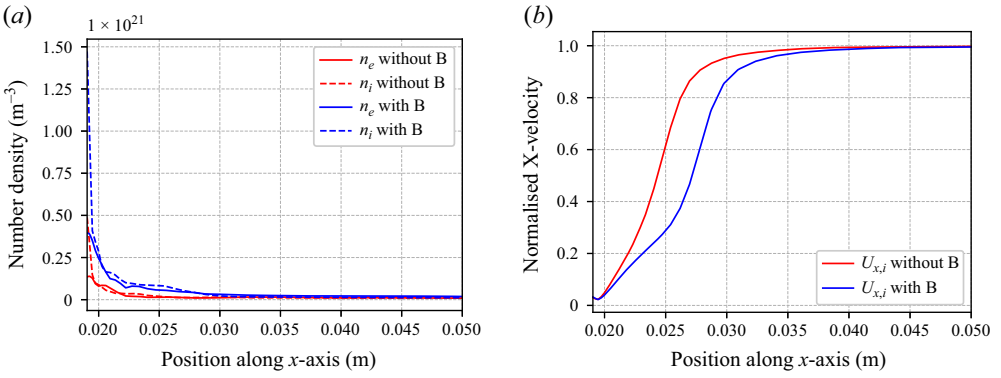


Figure 8. (*a*) Number density and (*b*) normalised x-velocity of ions along the stagnation line with and without applied magnetic field $B_{max} = 0.447$ T.

structure, shifting the primary electric field peak to the shoulder region. This redistribution is explained by Ohm's law, $\boldsymbol{E} \sim \boldsymbol{U} \times \boldsymbol{B}$, which indicates that the electric field peaks where the cross-product between the electron drift velocity and the magnetic field is maximised, as shown in figure 7(*a*). Figure 7(*e*) shows a strong current density concentrated in the stagnation region. The current density here is computed by $\boldsymbol{J} = q_i n_i \boldsymbol{U}_i + q_e n_e \boldsymbol{U}_e$. Figure 7(*i*) reveals a substantial Lorentz force near this area. The Lorentz force is computed as $\boldsymbol{F} = \boldsymbol{J} \times \boldsymbol{B}$. The force does not precisely align with the peak current density and magnetic field strength because the magnitude of the Lorentz force $\boldsymbol{J} \times \boldsymbol{B}$ is also critically dependent on the angle between the current density $\boldsymbol{J}$ and the magnetic field $\boldsymbol{B}$.

Figure 8(*b*) displays profiles of the normalised x-component velocity (U_x) for ions along the stagnation line (the reference velocity is the free stream velocity). The application of the magnetic field induces additional deceleration. This effect can be attributed to the magnetic mirror force, whereby the magnetic moment $\mu = m v_\perp^2/(2|\boldsymbol{B}|)$ – with $v_\perp$ representing the velocity perpendicular to the magnetic field – is approximately conserved in slowly varying fields (Lee, Kim & MacCormack 2015). As charged particles approach the wall, converging magnetic field lines convert perpendicular kinetic energy into parallel motion, resulting in deceleration along the stagnation line. The corresponding reorganisation of electron flow is illustrated in figure 10, where initially smooth streamlines (panel *a*) become disordered under magnetisation (panel *b*).

Figure 9 presents the normalised surface pressure and heat flux distributions for Ar, Ar^+ and e^-. The reference value for surface pressure and heat flux are $\rho_{Ar,\infty} U_\infty^2/2$ and $\rho_{Ar,\infty} U_\infty^3/2$, where ∞ represents free stream value. Figure 9(*a*) illustrates that the surface pressure of Ar increases near the stagnation region and decreases in the shoulder region. A similar trend in surface pressure is observed for Ar^+. Figure 9(*b*) shows a decrease in heat flux near the stagnation region for Ar, attributable to an enlarged standoff distance leading to a smaller temperature gradient. In contrast, the heat flux of Ar^+ increases in the stagnation region, potentially due to much higher number density near the wall surface caused by the magnetic field and direct energy input from the magnetic field. The pressure and heat flux distribution of e^- is similar to Ar^+. Given that the mole fraction of Ar^+ is only 0.00623, the overall surface pressure and heat flux are predominantly governed by Ar. The observed increase in stagnation pressure and decrease in heat flux on the hemisphere's surface are consistent with most established literature in this field (Bush 1958; Poggie & Gaitonde 2002; Fujino *et al.* 2008).

https://doi.org/10.1017/jfm.2026.11462 Published online by Cambridge University Press

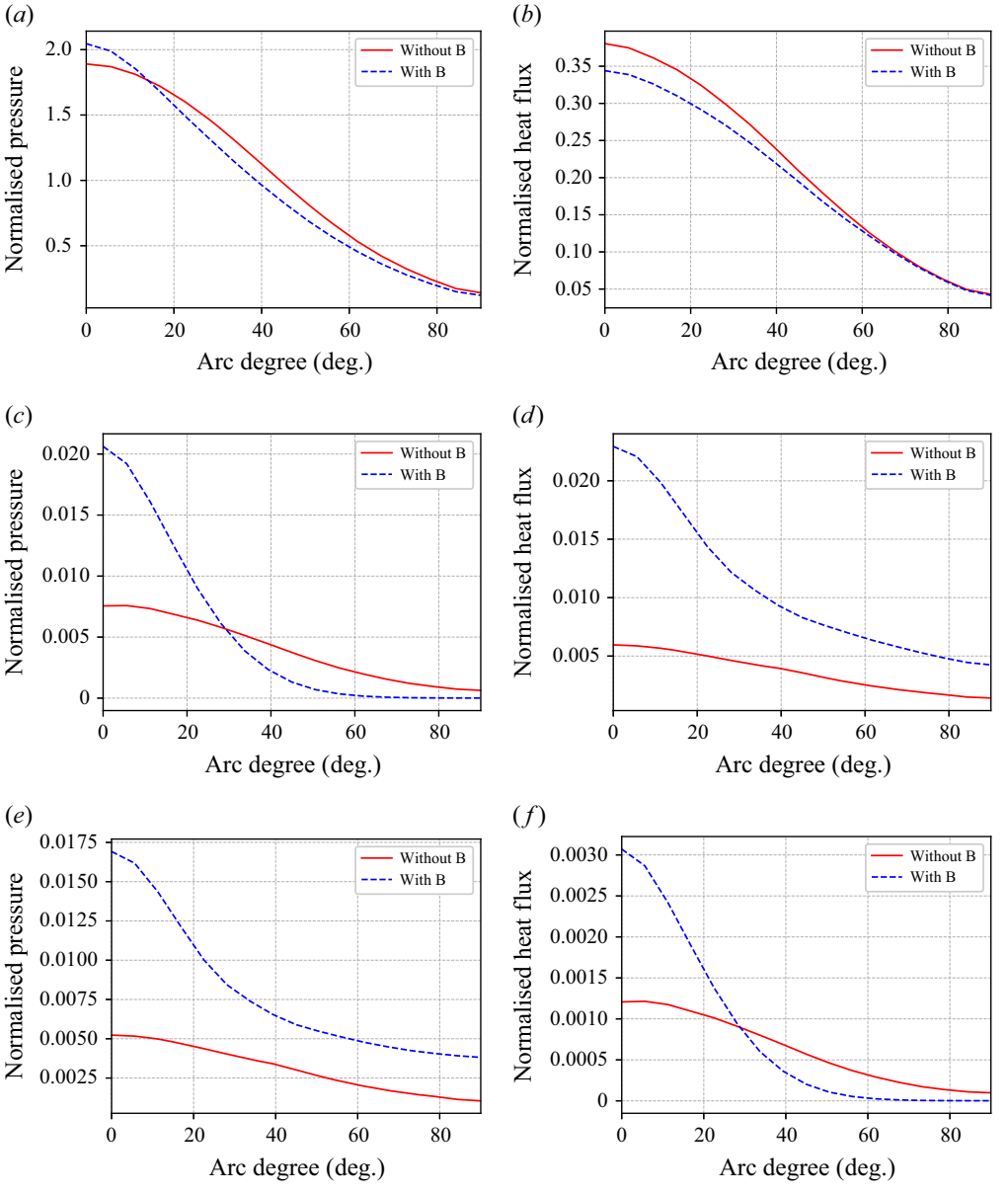


Figure 9. Normalised surface pressure of (*a*) Ar, (*c*) Ar^{+}, (*e*) e^{-} and surface heat flux of (*b*) Ar, (*d*) Ar^{+}, (*f*) e^{-} at $B_{max} = 0.447$ T.

The dependence of shock standoff distance on applied magnetic field strength is presented in figure 11. The shock front location is determined using the density jump ratio, which is defined as (Bisek *et al.* 2010)

$$\lim_{M_1 \to \infty} \frac{\rho_2}{\rho_1} = \frac{\gamma + 1}{\gamma - 1}. \tag{3.2}$$

Here, M_1 denotes the upstream Mach number, γ represents the ratio of specific heats, ρ_1 is the upstream density and ρ_2 is the downstream density. For argon gas, with $\gamma_{Ar} = 5/3$, this density ratio is calculated to be 4. Our simulations exhibit good agreement with

https://doi.org/10.1017/jfm.2026.11462 Published online by Cambridge University Press

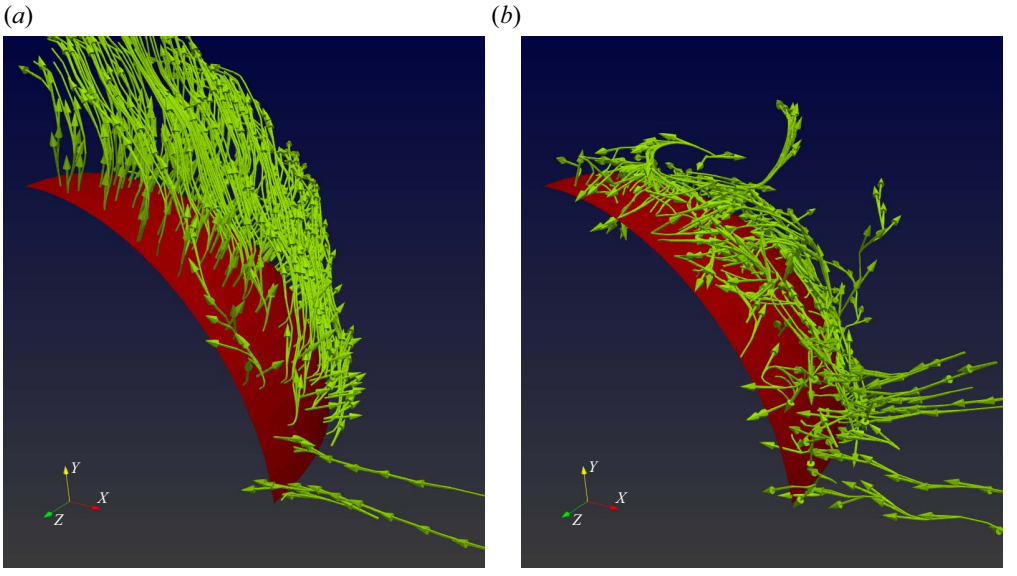


Figure 10. Streamline of electron near the wall (*a*) without magnetic field and (*b*) with magnetic field $B_{max} = 0.447$ T.

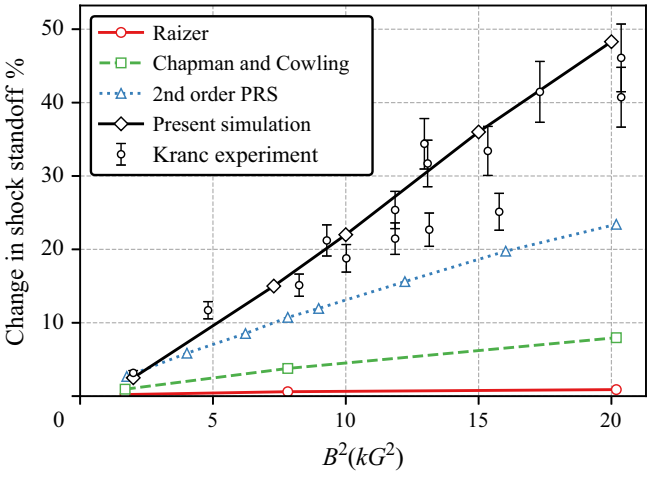


Figure 11. Changes in shock standoff distance as a function of magnetic field strength for Mach 4.75 pre-ionised argon flow around a hemispherical geometry (Cambel 1967) (experimental uncertainties is ±10 %).

experimental data. (The experimental uncertainty arises from limitations inherent in the measurement technology.) In addition to experimental results, reference simulation data from Bisek *et al.* (2010), employing three distinct conductivity models, are included for comparison. The primary distinction between the present formulation and Bisek's work lies in our consideration of non-equilibrium transport phenomena in ionised gases, whereas Bisek's results are based on the MHD equations. For hypersonic flow around a hemisphere, the standoff distance increases with increasing Knudsen number when rarefied effects are significant (Long *et al.* 2024).

https://doi.org/10.1017/jfm.2026.11462 Published online by Cambridge University Press

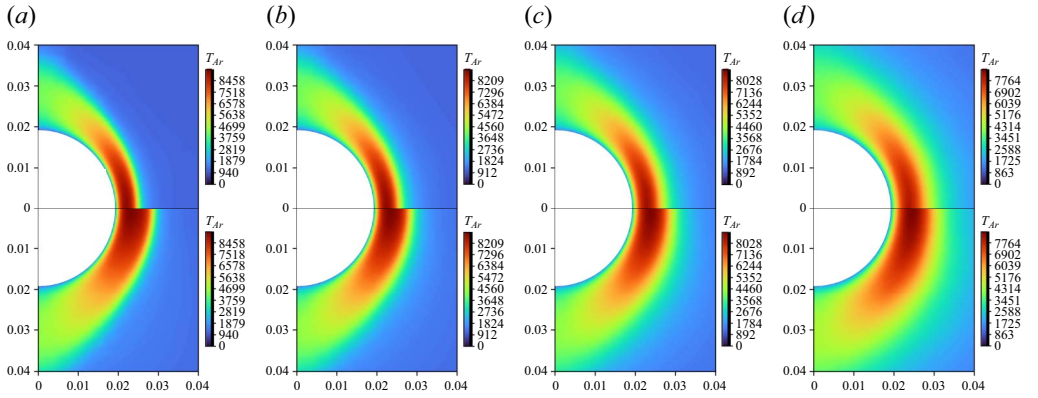


Figure 12. Temperature contour plots of the argon atoms at (*a*) $Kn = 0.02$, (*b*) $Kn = 0.04$, (*c*) $Kn = 0.08$, (*d*) $Kn = 0.2$ at $B_{max} = 0.447$ T. Upper and lower figures refer to the results without and with external magnetic fields.

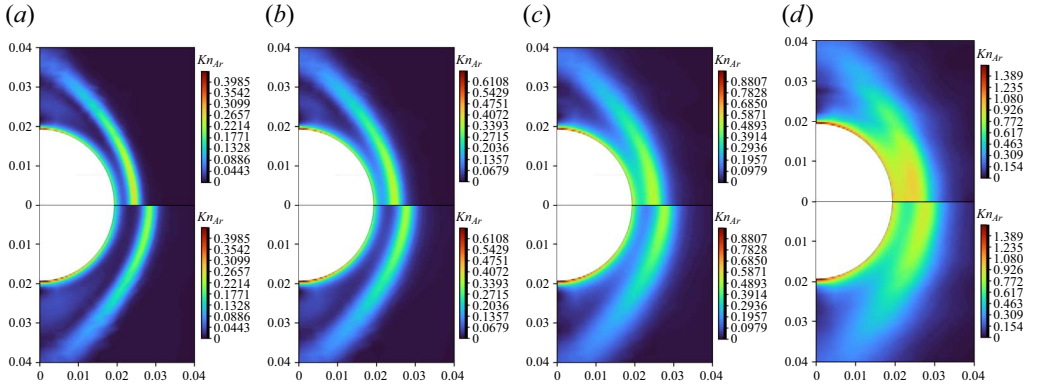


Figure 13. Local Knudsen number contour plots of the argon atoms at (*a*) $Kn = 0.02$, (*b*) $Kn = 0.04$, (*c*) $Kn = 0.08$, (*d*) $Kn = 0.2$ at $B_{max} = 0.447$ T. Upper and lower figures refer to the results without and with external magnetic fields.

3.2. *Control effects under different Knudsen numbers*

This subsection investigates the influence of control parameters across varying Knudsen numbers (0.2, 0.08, 0.044 and 0.02). The Knudsen number is determined by the incoming argon gas density, which is set to 2.18×10^{-5} kg m^{-3} for $Kn = 0.2$; 5.45×10^{-5} kg m^{-3} for $Kn = 0.08$; 1.09×10^{-4} kg m^{-3} for $Kn = 0.044$; and 2.18×10^{-4} kg m^{-3} for $Kn = 0.02$. The computational geometry, meshing and other detailed parameters remain the same as in the prior section. The similarity parameter, S, is held constant across these variations in Knudsen number. According to (A3) and (A5), shown in (A3), if the argon atom density increases by a factor a, the parameter S inherently decreases by a factor a^2. To counteract this effect and maintain a constant S, the magnetic field magnitude $|\boldsymbol{B}|$ must be amplified by the same factor a. The magnetic field magnitude in this section is set to be $B_{max} =$ 0.447 T.

Figure 12 displays the argon atom temperature field at various Knudsen numbers. The shock front exhibits a sharpening trend as the Knudsen number decreases. Figure 13 displays the local Knudsen number of an argon atom to illustrate the transport non-equilibrium of an argon atom. The local Knudsen number is defined as $Kn_{local} =$

https://doi.org/10.1017/jfm.2026.11462 Published online by Cambridge University Press

Knudsen number	Heat flux decrement
0.2	9.69 %
0.08	13.9 %
0.044	14.21 %
0.02	14.57 %

Table 3. Heat flux decrement with varying Knudsen number.

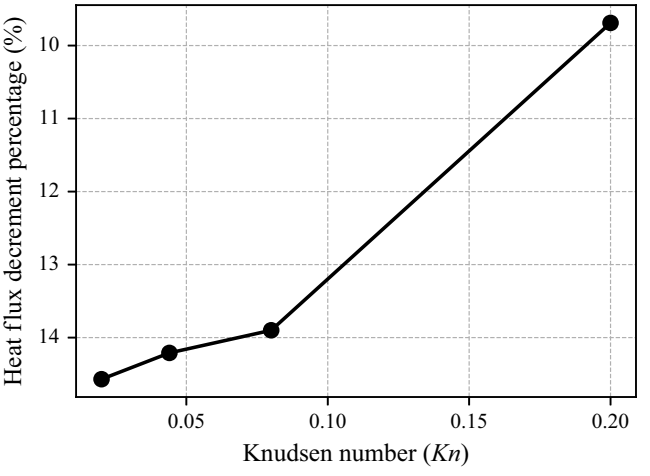


Figure 14. Heat flux decrement percentage as functions of the Knudsen number.

$\lambda/\rho/|\nabla\rho|$, where λ is local molecular mean free path; ρ is the mass density. The plot shows that the overall Knudsen number increases throughout the domain as the reference Knudsen number rises. In particular, at a higher Knudsen number as $Kn = 0.2$, the local Knudsen number inside the shock wave remains comparable in magnitude to that outside the shock, indicating a non-equilibrium state even within the shock region itself.

Figures 12 and 13 show that the standoff distance increment reduces with increasing Knudsen numbers. As a result, the total heat flux decrement also exhibits a decreasing trend with larger Knudsen numbers, as shown in table 3 and figure 14. The heat flux is calculated by integrating over the entire wall surface area. This phenomenon is due to the enhanced decoupling between atoms and charged particles at higher Knudsen numbers. The normalised x-velocity and temperature profiles along the stagnation line are shown in figures 16 and 15, respectively. The referenced values are free stream velocity and temperature. As illustrated, the velocity and temperature differences between atoms and ions grow progressively larger with increasing Knudsen number, reflecting a more pronounced departure from equilibrium. This trend arises from the inverse relationship between the Knudsen number and number density: at higher Knudsen numbers, lower atom densities reduce the collision frequency between atoms and ions. Conversely, as the Knudsen number decreases – corresponding to increased atom density – collisions become more frequent, driving the velocities and temperatures towards equilibrium.

Figure 17 presents the maximum velocity difference (panel *a*) and maximum temperature difference (panel *b*) between atoms and ions as functions of the Knudsen number. Both differences increase approximately linearly with the Knudsen number. This linear trend corresponds directly to the observed reduction in surface heat flux

https://doi.org/10.1017/jfm.2026.11462 Published online by Cambridge University Press

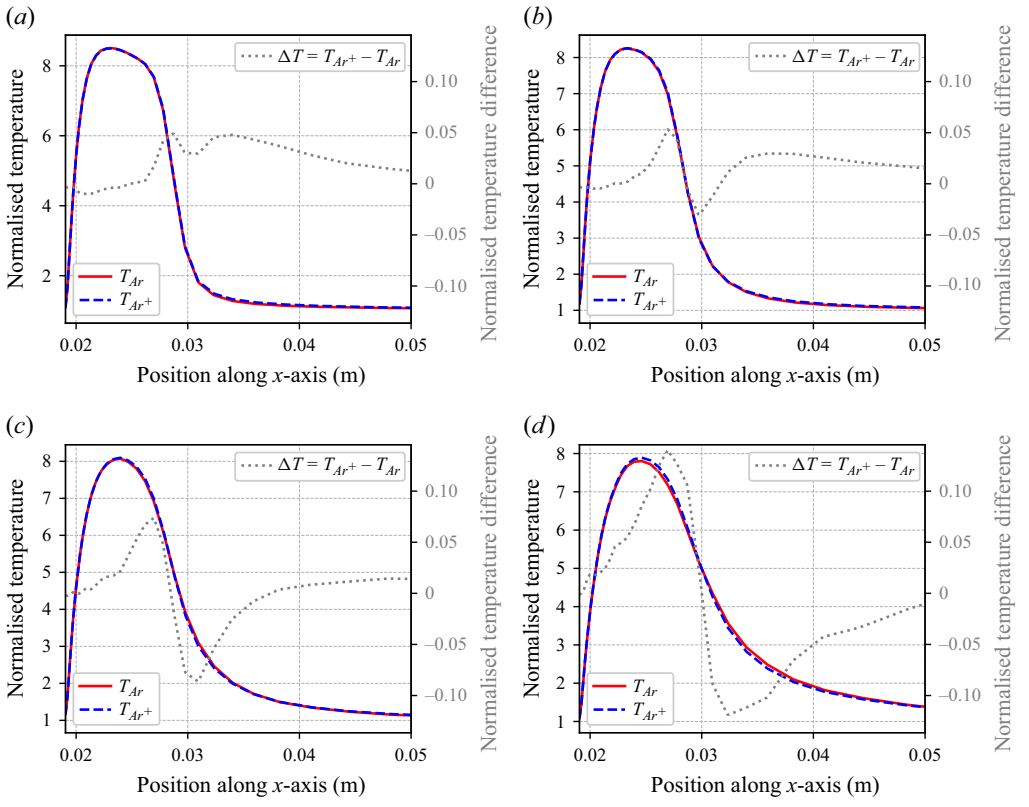


Figure 15. Normalised temperature profile of argon atom and argon ions along the stagnation line at (*a*) $Kn = 0.02$, (*b*) $Kn = 0.04$, (*c*) $Kn = 0.08$, (*d*) $Kn = 0.2$. The temperature difference $\Delta T = T_{Ar^+} - T_{Ar}$ is also shown as grey dots.

with increasing Knudsen number in figure 14, confirming that higher rarefaction leads to greater departure from equilibrium between charged and neutral species. Figure 18 further illustrates the x-velocity of argon atoms with and without an applied magnetic field. The magnetic field significantly decelerates the argon atoms, but the magnitude of this deceleration diminishes as the Knudsen number rises. Consistent with the previous discussion, the enhanced decoupling at higher *Kn* weakens the drag exerted by the charged species on the neutrals, thereby reducing the deceleration effect. This mechanism explains why higher Knudsen conditions attenuate the electromagnetic control effectiveness. In summary, increasing the Knudsen number enhances the decoupling between charged and neutral particles, which in turn weakens the efficacy of electromagnetic control.

4. Conclusions

This study applies the UGKWP method to multiscale simulations of partially ionised plasma flows around a hemisphere, spanning regimes from near-continuum to highly rarefied. Validation against experimental data for pre-ionised argon flows confirms the accuracy and robustness of the numerical implementation. A comparative investigation of control effects across different Knudsen numbers shows that rarefied effects can significantly alter predictions of electromagnetic flow control. Future work will extend the framework to include additional physical phenomena, such as wall sheath dynamics and comprehensive magnetohydrodynamic effects at moderate to high magnetic Reynolds

https://doi.org/10.1017/jfm.2026.11462 Published online by Cambridge University Press

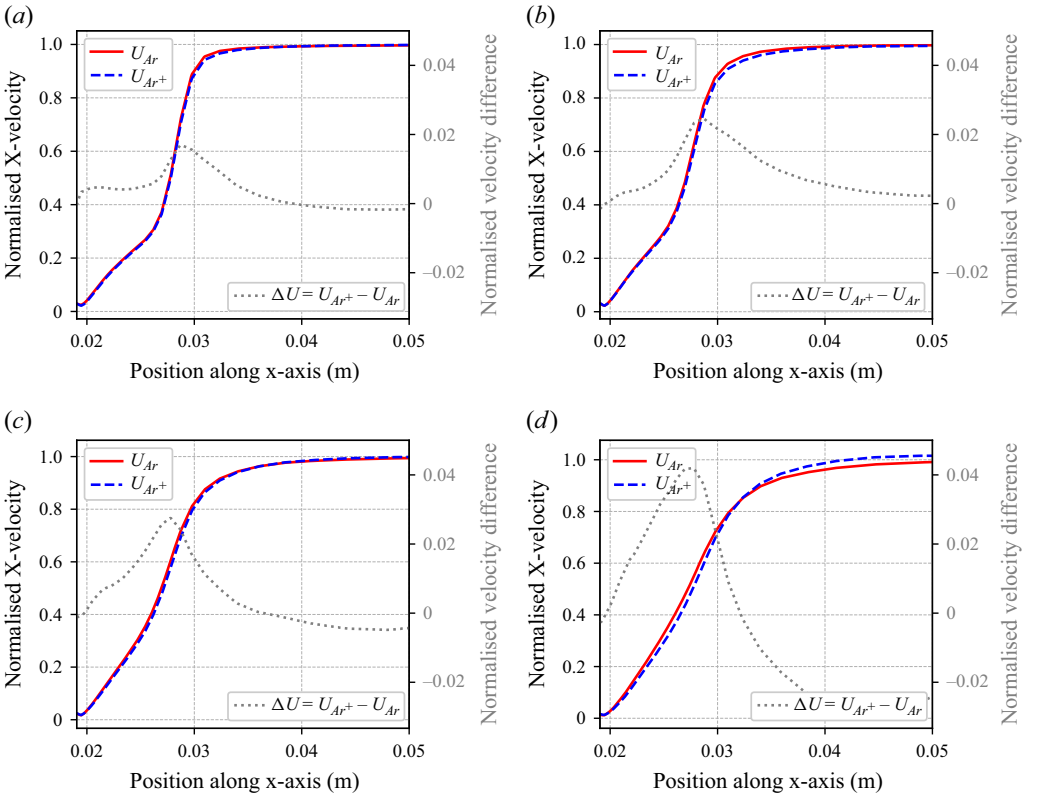


Figure 16. Normalised x-velocity profile of argon atom and argon ions along the stagnation line at (*a*) $Kn = 0.02$, (*b*) $Kn = 0.04$, (*c*) $Kn = 0.08$, (*d*) $Kn = 0.2$. The temperature difference $\Delta U_x = U_{Ar^+,x} - U_{Ar,x}$ is also shown as grey dots.

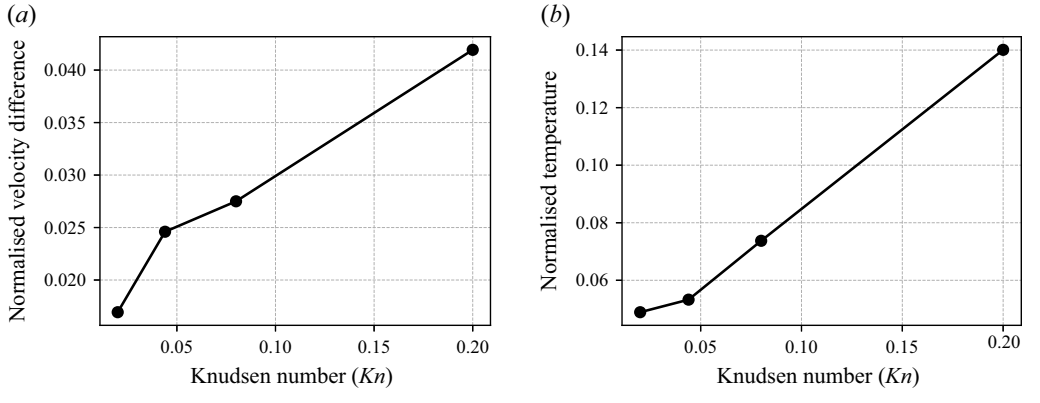


Figure 17. (*a*) Maximum normalised velocity difference and (*b*) maximum normalised temperature difference along the stagnation line between atoms and ions as functions of the Knudsen number.

numbers. The reliability of these advanced simulations will continue to rely on the robust multiscale flow-field solutions enabled by the UGKWP solver. Taken together, the present study establishes a solid foundation for advancing the simulation of complex plasma flow phenomena.

https://doi.org/10.1017/jfm.2026.11462 Published online by Cambridge University Press

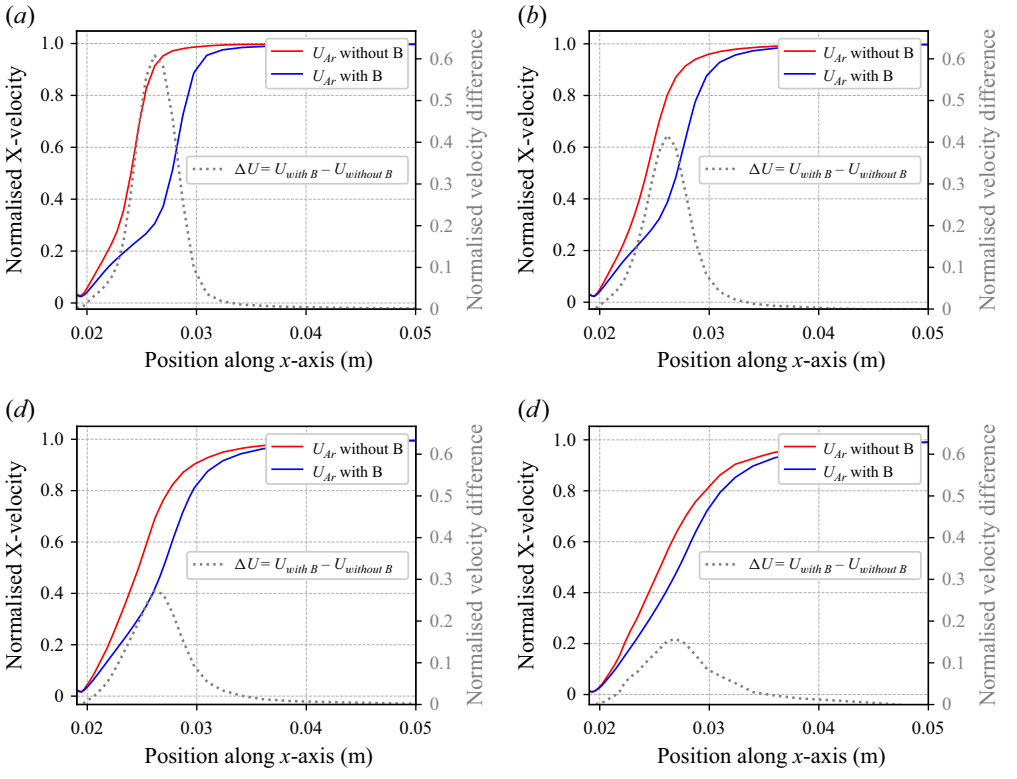


Figure 18. Normalised x-velocity profile of argon atom with and without the applied magnetic field along the stagnation line at (*a*) $Kn = 0.02$, (*b*) $Kn = 0.04$, (*c*) $Kn = 0.08$, (*d*) $Kn = 0.2$. The velocity difference is plotted as grey dots.

Acknowledgements. The first author would like to thank W. Long, J. Cao, H. Liu and S. Qin for their valuable discussions on the project.

Funding. This current work was supported by National Key R&D Program of China (Grant Nos. 2022YFA1004500), National Natural Science Foundation of China (92371107) and the Hong Kong Research Grant Council (16208324).

Declaration of interests. The authors report no conflict of interest.

Appendix A. Artificial electron mass effect

According to Drude's conductivity model (Yoshino, Fujino & Ishikawa 2010),

$$\sigma^{cond} = \frac{n_e e^2}{m_e \sum_{s \neq e} \nu_{e,s}}, \tag{A1}$$

where $\nu_{e,s}$ is the collision frequency between species s and electrons, and is given as (Chen *et al.* 1984)

$$\nu_{e,s} = n_s \sigma_{e,s}^{col} \bar{v}_{th}, \tag{A2}$$

where n_s is number density of species s; $\sigma_{e,s}^{col}$ is the cross-section between species s and electrons; and $\bar{v}_{th}$ is the average relative velocity between species s and electrons and is given approximately as the average velocities of electrons $\bar{v}_{th} = \sqrt{8 k_B T_e / \pi m_e}$. Therefore,

https://doi.org/10.1017/jfm.2026.11462 Published online by Cambridge University Press

the conductivity is given as

$$\sigma^{cond} = \frac{n_e e^2}{m_e \sum_{s \neq e} n_s \sigma_{e,s}^{col} \sqrt{\dfrac{8 k_B T_e}{\pi m_e}}}. \tag{A3}$$

In the current work, $\sigma_{e,s}^{col}$ is given by a fitted curve, and n_e, T_e and n_s are calculated by the flow field so their expressions do not contain m_e, then we have

$$\sigma^{cond} \propto \frac{1}{\sqrt{m_e}}, \tag{A4}$$

which means conductivity decreases as m_e increases. Standoff distance is proportional to the dimensionless magnetic interaction parameter (Poggie & Gaitonde 2002),

$$S = \frac{\sigma_0^{cond} |\boldsymbol{B}_0|^2 L_0}{\rho_0 |\boldsymbol{U}|_0}, \tag{A5}$$

where subscript 0 means characteristic quantities. To make S constant, $|\boldsymbol{B}_0|^2$ has to increase when the conductivity decreases. Given that the actual mass ratio of argon ions (Ar^+) to electrons (e^-) is approximately 72 811, while the ratio employed in this paper is 10, the electrical conductivity is consequently reduced by a factor of approximately 85, so $|\boldsymbol{B}_0|^2$ needs to be increased by a factor of 85 to maintain the desired similitude.

Appendix B. Discretisations of cross-species collision term

The discretised form of (2.38) is

$$\begin{aligned}
&\frac{\boldsymbol{U}_\alpha^{n+1} - \boldsymbol{U}_\alpha^{**}}{\Delta t} = \sum_{k=1}^{N} \frac{2 m_k \chi_{\alpha k} n_k}{m_\alpha + m_k} (\boldsymbol{U}_k^{n+1} - \boldsymbol{U}_\alpha^{n+1}), \\
&\frac{E_\alpha^{n+1} - E_\alpha^{**}}{\Delta t} = \sum_{k=1}^{N} \frac{2 m_k \chi_{\alpha k} n_k}{m_\alpha + m_k} \boldsymbol{U}_\alpha^{n+1} \left(\boldsymbol{U}_k^{n+1} - \boldsymbol{U}_\alpha^{n+1} \right) \\
&+ \sum_{k=1}^{N} \frac{4 m_k \chi_{\alpha k} n_k}{(m_\alpha + m_k)^2} \left[m_k \left(E_k^{n+1} - \frac{1}{2} \left(\boldsymbol{U}_k^{n+1} \right)^2 \right) - m_\alpha \left(E_\alpha^{n+1} - \frac{1}{2} \left(\boldsymbol{U}_\alpha^{n+1} \right)^2 \right) + \frac{m_k}{2} \left(\boldsymbol{U}_k^{n+1} - \boldsymbol{U}_\alpha^{n+1} \right)^2 \right].
\end{aligned} \tag{B1}$$

The Jacobian of residuals to velocity and energy is

$$\begin{aligned}
&\frac{\partial R_{U_\alpha}}{\partial \boldsymbol{U}_k} = \delta_{\alpha k} \left(\frac{1}{\Delta t} + \sum_{k=1}^{N} \frac{2 m_k \chi_{\alpha k} n_k}{m_\alpha + m_k} \right) - (1 - \delta_{\alpha k}) \left(\frac{2 m_k \chi_{\alpha k} n_k}{m_\alpha + m_k} \right), \\
&\frac{\partial R_{E_\alpha}}{\partial E_k} = \delta_{\alpha k} \left(\frac{1}{\Delta t} + \sum_{k=1}^{N} \frac{4 m_k m_\alpha \chi_{\alpha k} n_k}{(m_\alpha + m_k)^2} \right) - (1 - \delta_{\alpha k}) \frac{4 m_k^2 \chi_{\alpha k} n_k}{(m_\alpha + m_k)^2}, \\
&\frac{\partial R_{E_\alpha}}{\partial \boldsymbol{U}_k} = \delta_{\alpha k} \sum_{k=1}^{N} \frac{4 m_k \chi_{\alpha k} n_k}{(m_\alpha + m_k)^2} (-m_\alpha \boldsymbol{U}_\alpha + m_k (\boldsymbol{U}_k - \boldsymbol{U}_\alpha)) \\
&\quad + (1 - \delta_{\alpha k}) \left(\frac{4 m_k^2 \chi_{\alpha k} n_k}{(m_\alpha + m_k)^2} (\boldsymbol{U}_k - m_k (\boldsymbol{U}_k - \boldsymbol{U}_\alpha)) \right),
\end{aligned} \tag{B2}$$

https://doi.org/10.1017/jfm.2026.11462 Published online by Cambridge University Press

where

$$\delta_{\alpha k} = \begin{cases} 1 & \text{if } \alpha = k, \\ 0 & \text{else.} \end{cases} \tag{B3}$$

Residuals are

$$R_{U_\alpha} = \frac{\boldsymbol{U}_\alpha^{n+1} - \boldsymbol{U}_\alpha^{**}}{\Delta t} - \sum_{k=1}^{N} \frac{2m_k \chi_{\alpha k} n_k}{m_\alpha + m_k} \left(\boldsymbol{U}_k^{n+1} - \boldsymbol{U}_\alpha^{n+1} \right),$$

$$R_{E_\alpha} = \frac{E_\alpha^{n+1} - E_\alpha^{**}}{\Delta t} - \sum_{k=1}^{N} \frac{2m_k \chi_{\alpha k} n_k}{m_\alpha + m_k} \boldsymbol{U}_\alpha^{n+1} \left(\boldsymbol{U}_k^{n+1} - \boldsymbol{U}_\alpha^{n+1} \right)$$

$$+ \sum_{k=1}^{N} \frac{4m_k \chi_{\alpha k} n_k}{(m_\alpha + m_k)^2} \left[m_k \left(E_k^{n+1} - \frac{1}{2} \left(\boldsymbol{U}_k^{n+1} \right)^2 \right) - m_\alpha \left(E_\alpha^{n+1} - \frac{1}{2} \left(\boldsymbol{U}_\alpha^{n+1} \right)^2 \right) + \frac{m_k}{2} \left(\boldsymbol{U}_k^{n+1} - \boldsymbol{U}_\alpha^{n+1} \right)^2 \right]. \tag{B4}$$

The iterative solver is the Newton–Raphson method. Convergence is achieved when the relative change in the residual falls below a predefined tolerance, e_{tol}. Specifically, if the residual at iteration k is denoted as R^k and the residual at the preceding iteration $k-1$ is R^{k-1}, convergence is declared when $|R^k - R^{k-1}| < e_{tol}$.

References

Andries, P., Aoki, K. & Perthame, B. 2002 A consistent bgk-type model for gas mixtures. *J. Stat. Phys.* **106**, 993–1018.

Bird, G.A. 1976 Molecular gas dynamics. *NASA STI/Recon Techn. Rep. A* **76**, 40225.

Bisek, N.J., Boyd, I.D. & Poggie, J. 2010 Numerical study of magnetoaerodynamic flow around a hemisphere. *J. Spacecraft Rockets* **47** (5), 816–827.

Bisi, M., Boscheri, W., Dimarco, G., Groppi, M. & Martalò, G. 2022 A new mixed boltzmann-bgk model for mixtures solved with an imex finite volume scheme on unstructured meshes. *Appl. Math. Comput.* **433**, 127416.

Boyd, I.D. & Schwartzentruber, T.E. 2017 *Nonequilibrium Gas Dynamics and Molecular Simulation*, vol. 42. Cambridge University Press.

Bush, W.B. 1958 Magnetohydrodynamic-hypersonic flow past a blunt body. *J. Aerosp. Sci.* **25** (11), 685–690.

Cambel, A. 1967 Experimental investigation of magnetoaerodynamic flow around blunt bodies. In *6th Electric Propulsion and Plasmadynamics Conference*, p. 729.

Cambel, A.B. & Porter, R.W. 1967 Hall effect in flight magnetogasdynamics. *AIAA J.* **5** (12), 2208–2213.

Cao, J., Wei, Y., Long, W., Zhong, C. & Xu, K. 2026 Adaptive criterion and modification of wave-particle decomposition in ugkwp method for high-speed flow simulation. *Comput. Fluids* **305**, 106896.

Chen, F.F. *et al.* 1984 *Introduction to Plasma Physics and Controlled Fusion*, vol. 1. Springer.

Devoto, R.S. 1973 Transport coefficients of ionized argon. *Phys. Fluids* **16** (5), 616–623.

Fawley, D.M., Putnam, Z.R., D'Souza, S. & Borner, A. 2022 Assessment of electrical conductivity in rarefied flow about mars entry vehicles. *AIAA SCITECH 2022 Forum* 0825.

Fujino, T., Yoshino, T. & Ishikawa, M. 2008 Numerical analysis of reentry trajectory coupled with magnetohydrodynamics flow control. *J. Spacecraft Rockets* **45** (5), 911–920.

Guo, Z., Li, J. & Xu, K. 2023 Unified preserving properties of kinetic schemes. *Phys. Rev. E* **107** (2), 025301.

Jin, X., Peng, S. & Feng, Y. 2025 Numerical study on near-continuum hypersonic magnetohydrodynamic flow over blunt body. *AIAA J.* 1–8. 10.2514/1.J065695

Kai, L., Jun, L. & Weiqiang, .L. 2017 Thermal protection performance of magnetohydrodynamic heat shield system based on multipolar magnetic field. *Acta Astronaut.* **136**, 248–258.

Katsurayama, H., Kawamura, M., Matsuda, A. & Abe, T. 2008 Kinetic and continuum simulations of electromagnetic control of a simulated reentry flow. *J. Spacecraft Rockets* **45** (2), 248–254.

Lani, A., *et al.* 2023 A magnetohydrodynamic enhanced entry system for space transportation: meesst. *J. Space Safety Engng* **10** (1), 27–34.

Lee, J.K., Kim, T. & MacCormack, R.W. 2015 Simulation of hypersonic flow within electromagnetic fields for heat flux mitigation. In *20th AIAA International Space Planes and Hypersonic Systems and Technologies Conference*, p. 3503.

https://doi.org/10.1017/jfm.2026.11462 Published online by Cambridge University Press

LI, Q., ZENG, J. & WU, L. 2024 Kinetic modelling of rarefied gas mixtures with disparate mass in strong non-equilibrium flows. *J. Fluid Mech.* **1001**, A5.
LIU, C., LI, W., WANG, Y., SONG, P. & XU, K. 2023 An implicit unified gas-kinetic wave–particle method for radiative transport process. *Phys. Fluids* **35** (11), 112013.
LIU, C. & XU, K. 2021 Unified gas-kinetic wave-particle methods iv: multi-species gas mixture and plasma transport. *Adv. Aerodyn.* **3**, 1–31.
LIU, C., ZHU, Y. & XU, K. 2020 Unified gas-kinetic wave-particle methods i: continuum and rarefied gas flow. *J. Comput. Phys.* **401**, 108977.
LIU, H., YANG, X., ZHANG, C., JI, X. & XU, K. 2025 Unified gas-kinetic wave-particle method for multi-scale phonon transport. arXiv preprint arXiv: 2505.09297.
LONG, W., WEI, Y. & XU, K. 2024 Nonequilibrium flow simulations using unified gas-kinetic wave-particle method. *AIAA J.* **62** (4), 1411–1433.
MORSE, T.F. 1963 Energy and momentum exchange between nonequipartition gases. *Phys. Fluids* **6** (10), 1420–1427.
MUNZ, C.-D., OMNES, P., SCHNEIDER, R., SONNENDRÜCKER, E. & VOSS, U. 2000 Divergence correction techniques for maxwell solvers based on a hyperbolic model. *J. Comput. Phys.* **161** (2), 484–511.
PARENT, B., RAJENDRAN, P.T., MACHERET, S.O., LITTLE, J., MOSES, R.W., JOHNSTON, C.O. & CHEATWOOD, F.M. 2023 Effect of plasma sheaths on earth-entry magnetohydrodynamics. *J. Thermophys. Heat Transfer* **37** (4), 845–857.
POGGIE, J. & GAITONDE, D.V. 2002 Magnetic control of flow past a blunt body: numerical validation and exploration. *Phys. Fluids* **14** (5), 1720–1731.
PU, Z., LIU, C. & XU, K. 2024 Gas-kinetic scheme for partially ionized plasma in hydrodynamic regime. *J. Comput. Phys.* **505**, 112905.
PU, Z. & XU, K. 2025 Unified gas-kinetic wave-particle method for multiscale flow simulation of partially ionized plasma. *J. Comput. Phys.* **530**, 113918.
RESLER, E.L.Jr & SEARS, W.R. 1958 The prospects for magneto-aerodynamics. *J. Aerosp. Sci.* **25** (4), 235–245.
WEI, Y., CAO, J., JI, X. & XU, K. 2023 Adaptive wave-particle decomposition in ugkwp method for high-speed flow simulations. *Adv. Aerodyn.* **5** (1), 25.
YANG, X., SHYY, W. & XU, K. 2022 Unified gas-kinetic wave–particle method for gas–particle two-phase flow from dilute to dense solid particle limit. *Phys. Fluids* **34** (2), 023312.
YANG, X., SHYY, W. & XU, K. 2024 Unified gas-kinetic wave–particle method for polydisperse gas–solid particle multiphase flow. *J. Fluid Mech.* **983**, A37.
YANG, X., ZHU, Y., LIU, C. & XU, K. 2025 Unified gas-kinetic wave-particle method for frequency-dependent radiation transport equation. *J. Comput. Phys.* **522**, 113587.
YOSHINO, T., FUJINO, T. & ISHIKAWA, M. 2010 Numerical study of thermal protection utilizing magnetohydrodynamic technology in super-orbital reentry flight. In *41st Plasmadynamics and Lasers Conference*, p. 4486.
ZHU, Y., LIU, C., ZHONG, C. & XU, K. 2019 Unified gas-kinetic wave-particle methods. II. Multiscale simulation on unstructured mesh. *Phys. Fluids* **31** (6), 067105.
ZIEMER, R.W. & BUSH, W.B. 1958 Magnetic field effects on bow shock stand-off distance. *Phys. Rev. Lett.* **1** (2), 58.

https://doi.org/10.1017/jfm.2026.11462 Published online by Cambridge University Press